#### **Review Article**

Ekaterina Pecherskaya\*, Pavel Golubkov, Sergey Konovalov, Sergey Gurin, and Maksim Novichkov

# Mechanism, models, and influence of heterogeneous factors of the microarc oxidation process: A comprehensive review

https://doi.org/10.1515/rams-2024-0083 received April 07, 2024; accepted December 19, 2024

Abstract: The shortcomings of the microarc oxidation (MAO) technology are revealed, in accordance with which a range of topical scientific problems that need to be solved is formulated. It is shown that, despite significant progress in this area of research, there are still controversial issues related mainly to the features of the emergence and combustion of microdischarges. In order to develop a scientifically substantiated approach to the choice of the optimal mode for deposition of microarc oxide coatings, regularities in the influence of heterogeneous factors on their properties are systematized. The analysis of scientific works devoted to the mathematical description of the MAO process has been carried out. It is shown that the existing mathematical models have limitations, and are applicable only to certain aspects of coating formation and do not describe the MAO process as a whole. The prerequisites, recommendations, and theoretical provisions that can be used in the development of a complex mathematical model of the MAO process are revealed. Known methods of analytical description of the forming curve are considered. The possibility of using the forming curve for determining the correct choice of technological parameters and predicting the oxide coating properties during their formation is shown.

**Keywords:** microarc oxidation, mechanism of coating formation, mathematical models, influence of heterogeneous factors, prediction of coating properties, forming curve

#### 1 Introduction

At present, a promising way to modify the surface of light metals and alloys is microarc oxidation (MAO) [1-3] also known as plasma electrolytic oxidation (PEO), anodic spark deposition, plasma chemical oxidation, or anodic oxidation by spark discharge (German: Anodische Oxidation unter Funkenentladung) [4-6]. This technology makes it possible to synthesize on the sample surface oxide coatings with special properties: high hardness, wear resistance [7], corrosion resistance [8], heat resistance [9,10], adhesion to the substrate [11], and electric strength. Under certain conditions of obtaining MAO coatings on titanium may also have high biocompatibility [12,13] and antibacterial properties [14]. It depends on the electrolyte composition in which the MAO process was conducted and the properties of the coatings themselves. The scope of microarc oxide coating use covers industries such as mechanical engineering and transport, aviation, rocket and space technology, instrumentation, electronics, medicine [4], and it is constantly expanding. For example, the phenomenon of thermally stimulated luminescence discovered by Zolotarjovs et al. [15] opens up the possibility of using MAO coatings as detectors of ionizing radiation; the electrolyte composition proposed in the study by Wu et al. [16] makes it possible to obtain MAO coatings consisting of ferroelectric ceramics (barium titanate). MAO coatings of magnesium alloys are used as a sublayer for the deposition of catalytically active composite materials [17]. MAO coatings with high absorption coefficients of electromagnetic radiation in the terahertz range and in the near infrared spectrum, which can be used in the development of a new type of stealth technology [18], as well as optically black light-absorbing coatings for products of rocket and space technology [19] have been obtained. Saji [20] developed MAO coatings that are not subject to icing due to hydrophobic properties. In addition, MAO treatment can significantly improve the corrosion resistance of titanium dental implants modified with polyeugenol [21].

<sup>\*</sup> Corresponding author: Ekaterina Pecherskaya, Department of Metrology and Information and Measuring Technology, Penza State University, Penza, Russian Federation, e-mail: pea1@list.ru Pavel Golubkov, Sergey Konovalov, Sergey Gurin, Maksim Novichkov: Department of Metrology and Information and Measuring Technology, Penza State University, Penza, Russian Federation

Despite the progress made in improving the performance and searching for new applications of MAO coatings, there are currently several unresolved problems in MAO technology. From a practical point of view, the most important problem is the high energy intensity of the MAO process. As shown by Troughton et al. [22], a negligibly small part of the input power of the process current source is spent directly on the formation of MAO coatings; the rest of the energy is spent on side processes, mainly on heating the electrolyte. The energy consumption of the process depends on the parameters of the technological regime, which, as a rule, are determined empirically in the course of production preparation. In the case of the MAO process, the empirical selection of optimal technological parameters is difficult due to the influence of many heterogeneous factors on the properties of the resulting coatings [23-27]. Establishment and analytical description of the dependences of the MAO coating properties on the influencing factors of the MAO process is the second important task that needs to be solved.

From a theoretical point of view, the most significant problem is the insufficient knowledge of the MAO process. The process of coating formation has a complex interdisciplinary nature and combines many phenomena from the field of electrochemistry, plasma physics, thermodynamics, and materials science [28–30]. It is with insufficiently deep understanding of the mechanism of coating formation that the previously considered practical problems are associated. As noted in the study by Troughton et al. [22], in order to develop scientifically based methods for increasing the energy efficiency of the MAO process, a more detailed study of the mechanism of coating formation, in particular, physicochemical processes at the solid-liquid and solid-gas interface during a discharge in a liquid [31] is necessary. Clyne and Troughton [28] state that at present the fundamental theory of plasma electrolysis has not been developed. All this emphasizes the relevance of solving the identified scientific and practical problems.

Currently, a promising area of mathematical modelling of complex interdisciplinary systems and technological processes is the creation of digital twins [32]. As a rule, such models are based on artificial intelligence algorithms that can process large amounts of information and allow solving complex problems under uncertainty conditions. However, errors are also possible in the operation of such algorithms, *e.g.*, those associated with the incorrectness of the training set [33,34]. Therefore, when developing digital twins, in addition to intelligent algorithms, one should also use traditional mathematical models that describe the properties of the object of study using physical laws. It should also be noted that digital twins have not yet been developed for the MAO process.

Thus, the systematization of the available data on the mechanism of the MAO process, influencing heterogeneous factors, physical principles, and theories used in the analytical description of the coating formation process, will allow us to identify the most promising of them and use them in the development of a generalized mathematical model that can serve as the basis for a digital twin of the MAO process.

The presented work consists of five parts. Section 1 substantiates the relevance of the study, identifies problems and ways to solve them. Section 2 provides brief theoretical information about the MAO process, the materials used, electrolytes, and modes. Section 3 provides information on the mechanism of coating formation and analyzes various versions of its interpretation. In Section 4, the question of the influence of heterogeneous factors on the MAO coating properties is considered, and the regularities of this influence are systematized. In Section 5, methods of mathematical description of the coating formation process are considered, and recommendations for their use in the development of a complex mathematical model underlying the digital twin of the MAO process are given. In Section 6, the work results are formulated.

### 2 Essence of the MAO process

MAO is a complex plasma-chemical process for the formation of an oxide coating on the surface of a sample, usually made of valve metal [35]. MAO is carried out in a twoelectrode galvanic cell filled with an electrolyte, the coated sample serves as an anode [36]. The most common MAO electrolyte is silicate-alkaline, consisting of NaOH or KOH and sodium silicate Na<sub>2</sub>SiO<sub>3</sub>. However, MAO treatment in acid electrolytes, suspension electrolytes, etc., is possible [37–39]. In order to impart new properties to MAO coatings (improve performance), nanoparticles, including graphene and carbon nanotubes, are added to the electrolyte [40-42]. The most common electrolyte compositions and MAO modes are given in Table 1. The process proceeds on alternating current (pulsed [54], rarely sinusoidal [22]) at high voltage (up to 1,000 V) and current densities up to 50 A·dm<sup>-2</sup>. In this case, it is considered that in the anode (positive) half-cycle of the technological current, the coating increases, and in the cathode (negative) half-cycle, it dissolves [55]. A distinctive feature of the MAO process is the presence of microdischarges burning on the anode surface, under the action of which the formed amorphous metal oxide of the base undergoes a phase transition into crystalline modifications (corundum for aluminum, anatase for titanium, etc.), which

Table 1: Most common electrolyte compositions and MAO modes

Substrate material	Electrolyte	Mode	Processing result	Ref.
Aluminum, titanium	$Na_2B_4O_7\cdot 10H_2O$ and $Na_2HPO_4\cdot 12H_2O$ with additions of $Co(CH_3COO)_2,~K_3[Fe(CN)_6],~and~Ni(OH)_2$	Amplitude voltage 300–400 V, pulse duration 100 µs, processing time 5–15 min; neodymium magnetization	An MAO coating capable of absorbing electromagnetic radiation in the near and mid-IR range has been obtained	[43]
Titanium	5 g·L <sup>-1</sup> Na <sub>3</sub> PO <sub>4</sub> , 2 g·L <sup>-1</sup> KOH	Anode pulse (frequency 50 Hz, duty cycle 90%). Processing time 6 min	Hydrophobic coating with high corrosion resistance is obtained	[44]
Ti-42Al-2V-2Nb	(1) 5 g·L <sup>-1</sup> Na <sub>2</sub> SiO <sub>3</sub> , 2.5 g·L <sup>-1</sup> KOH; (2) 5 g·L <sup>-1</sup> Na <sub>3</sub> PO <sub>4</sub> , 2.5 g·L <sup>-1</sup> KOH; (3) 2.5 g·L <sup>-1</sup> Na <sub>2</sub> SiO <sub>3</sub> , 2.5 g·L <sup>-1</sup> Na <sub>3</sub> PO <sub>4</sub> , 2.5 g·L <sup>-1</sup> KOH	Anode pulse mode, pulse frequency 1kHz, current density 170 mA·cm <sup>-2</sup> , processing time 12 min	Improving the corrosion resistance of coatings	[45]
Ti-18Zr-15Nb	20 g·L <sup>-1</sup> Na <sub>3</sub> PO <sub>4</sub> ·12H <sub>2</sub> O	Bipolar pulse mode, anode voltage 470 V, cathode – 40 V. The pulse frequency is 300 Hz, the duty cycle of the anode half-cycle is 51%, cathode – 26%. Processing time 5 min, electrolyte temperature 20 + 1 °C	Increased corrosion resistance and biocompatibility	[46]
Magnesium	15 g·L <sup>-1</sup> Na <sub>3</sub> PO <sub>4</sub> ·12H <sub>2</sub> O, 2 g·L <sup>-1</sup> Ca(OH) <sub>2</sub> , 5 g·L <sup>-1</sup> Sr (OH) <sub>2</sub> ·8H <sub>2</sub> O	Pulse anode galvanostatic mode, amplitude voltage 500 V, pulse frequency 2 kHz, duty cycle 20%, current density is 0.02 A·cm <sup>-2</sup> for 30 s, and 1 A·dm <sup>-2</sup> for 10 min	Extending the life of coated magnesium prostheses	[47]
Mg <sub>0.8</sub> Ca	CaSiO <sub>3</sub> , NaOH, Na <sub>2</sub> SiO <sub>3</sub> , NaF	Anode potentiostatic mode, amplitude voltage 350–500 V, processing time 5 min	The toxicity of the alloy is reduced	[48]
AZ63	$10~\mathrm{g}\cdot\mathrm{L}^{-1}~\mathrm{NaAlO}_2$	Pulse galvanostatic mode, amplitude voltage 570 V, current 2A (current density 0.23 A·cm <sup>-2</sup> ), frequency 150 Hz, average duty cycle 42%, processing time 5.20 min, electrolyte removature below 300°C	Corrosion resistance increases by two-orders of magnitude, microhardness by five times	[49]
AZ31	10 g·L <sup>-1</sup> NaAlO <sub>2</sub> , 10 g·L <sup>-1</sup> Na <sub>2</sub> WO <sub>4</sub> ·2H <sub>2</sub> O, 3 g·L <sup>-1</sup> C <sub>6</sub> H <sub>8</sub> O <sub>7</sub> ·H <sub>2</sub> O, 2 g·L <sup>-1</sup> KOH	Pulse bipolar and unipolar modes; average current density: anode 0.22 A·cm <sup>-2</sup> , cathode 0.09 A·cm <sup>-2</sup> , pulse frequency: 10, and 2 000 Hz; club cycle 20% processing time 480 s	Obtaining optically black coatings	[20]
WE43	15 g·L <sup>-1</sup> Na <sub>2</sub> SiO <sub>3</sub> , 13 g·L <sup>-1</sup> kF, 2 g·L <sup>-1</sup> ·NaOH	Bipolar pulse galvanostatic mode with an amplitude voltage of 450 V, a frequency of 700 Hz and a duty cycle of 20%.	Increased corrosion resistance	[51]
WE43	(1) 3 g·L <sup>-1</sup> KOH, 8 g·L <sup>-1</sup> B <sub>5</sub> H <sub>10</sub> NaO <sub>13</sub> ; (2) 8 g·L <sup>-1</sup> NaAlO <sub>2</sub> , 8 g·L <sup>-1</sup> B <sub>5</sub> H <sub>10</sub> NaO <sub>13</sub>	Bipolar pulse mode, anode voltage 420 V, cathode voltage 100 V. frequency 500 Hz. Processing time 15 min	Increased wear resistance of coatings	[52]
Tantalum	2–10 g·L <sup>-1</sup> NaAlO <sub>2</sub> , 2 g·L <sup>-1</sup> KOH	Pulse bipolar mode, pulse frequency 1 kHz, duty cycle 20%, average anode and cathode current densities are ~0.22 and ~0.11 A·cm <sup>-2</sup> , respectively. Processing time 20 or 60 min	Amorphous MAO coating with high corrosion resistance is obtained	[53]

alloy). Mg0.8Ca: 99.2 wt% Mg and 0.8 wt% Ca (bioresorbable magnesium alloy). AZ63: 5-7 wt% Al, 2-4 wt% Zn, 0.15 wt% Mn, 0.1 wt% Cu, 0.3 wt% Si, 0.003 wt% Fe, 0.003 wt% Ni, 0.3 wt% others, and balance Mg (Mg-Al alloy). AZ31: 3.05 wt% Al, 0.82 wt% Zn, 0.4 wt% Mn, 0.02 wt% Si, 0.003 wt% Cu, 0.0012 wt% Ni, 0.0023 wt% Fe, and balance Mg (extruded Mg-Al alloy). WE43: 3.7-4.3 wt% Y, 2.4-4.4 wt% Rare Alloy compositions from Table 1: Ti-42Al-2V-2Nb: 42 at% Al, 2 at% V, 2 at% Nb, and balance Ti (Ti-Al-V alloy). Ti-18Zr-15Nb: 18 at% Zr, 15 at% Nb, and balance Ti (Ti-Zr-Nb biocompatible shape-memory Earths, 0.4 wt% Zr, and balance Mg (high-strength magnesium alloy).

gives the coating special properties: high hardness, heat resistance, and electric strength [56,57]. In this case, the temperature in the channel of microarc discharges can reach 8,000 K [31]. Microdischarges are accompanied by a characteristic crackling caused by the collapse of gas-vapor bubbles formed in the coating pores, and the intensity of this cracking changes as the oxide increases. When gas-vapor bubbles collapse, the coating particles can be thrown into the electrolyte under the action of shock waves and lead to clogging of the electrolyte with sludge, which reduces its service life. The same negative effect is created when the electrolyte is depleted of ions during long-term operation (the so-called "depletion"), which is due to the fact that some of the ions are part of the formed coating. The third undesirable effect is the coating destruction by powerful arc discharges during excessively long deposition of coatings.

The coating formed by MAO consists of three layers: barrier (or transition), working (or functional), and porous (technological) (Figure 1) [58]. The transition layer is located at the "metal-coating" interface and is characterized by a gradual decrease in the concentration of oxides when moving toward the substrate. The working layer, which has the greatest thickness, contains predominantly crystalline oxides and is characterized by increased performance. The technological layer contains oxides of both the substrate metal and electrolyte components and has a high porosity [59]. For most technical applications, this layer is usually removed during mechanical processing; however, it can be used as catalyst carriers and biocompatible coatings in medicine [36,60,61]. The barrier and porous layers consist of amorphous oxides.

It should be noted that at present the range of materials subjected to MAO processing has expanded significantly. Traditionally, these materials include metals of the valve group, which in the "metal-oxide-electrolyte" system have one-sided conductivity. Among them, aluminum, magnesium, titanium, and their alloys [62–64] have the greatest practical

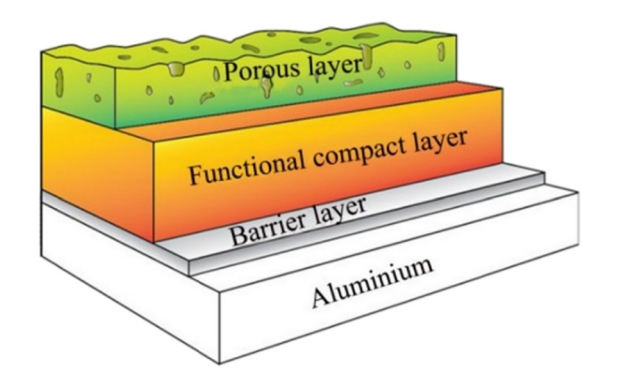
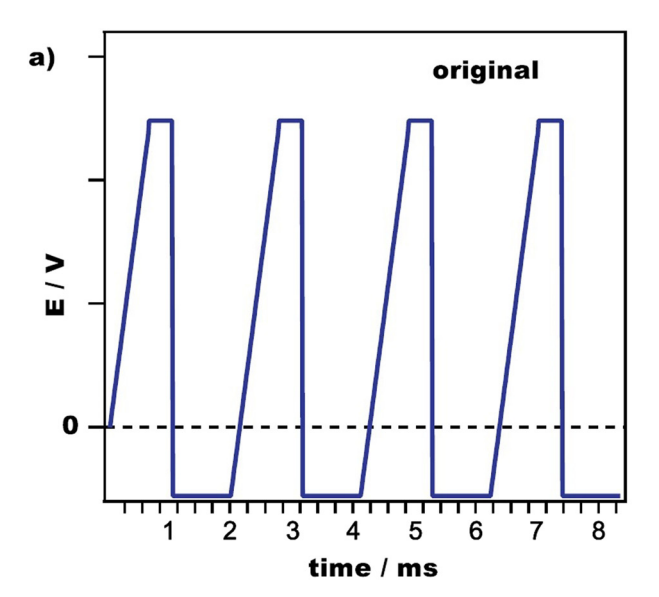


**Figure 1:** The structure of the MAO coating (using the example of aluminum) [58].

application while tantalum [53], zirconium [65], or niobium has lesser application [66]. However, in recent years, the number of publications devoted to the MAO of non-valve metals (mainly zinc [67,68] copper, and their alloys [69], sometimes iron [70]) has increased, which until recently was considered theoretically impossible.

There are also modifications of the MAO process. For example, a two-step MAO processing method is proposed, which consists of the following. At the first stage, MAO of a magnesium alloy is carried out in an alkaline-phosphatealuminate electrolyte until a coating up to 20 µm thick is obtained, and then the process continues in an alkaline electrolyte with a high concentration of sodium silicate. This MAO method makes it possible to increase the corrosion resistance due to the formation of a denser inner layer of coatings [55]. The modes of coating formation are developed, which differ in the shape of the technological impact signal. In the first of them, asymmetric high-voltage pulses of a special shape are applied to the sample, the characteristic feature of which is a slow rise in the leading edge and a sharp decline in the trailing edge of the pulse [71,72]. The second mode differs from the first one in that an additional voltage pulse is formed at the peak of the anode pulse, the duration of which is shorter than that of the main one (Figure 2). The second variant of the technological mode makes it possible, other things being equal, to obtain a smoother coating with an ultrafine microstructure [71]. In addition, it is possible to combine MAO with other coating technologies, e.g., to form oxide layers on steel parts. In this case, first, a layer of aluminum is applied to the steel part by cold gas-dynamic spraying, then it is subjected to MAO treatment in order to harden the surface, and then a layer of fluoroplast is applied by magnetron sputtering in order to improve anticorrosion properties. Such treatment leads to a significant increase in the wear resistance of the resulting coatings (by a factor of 3.1-3.3 compared to unhardened samples) [73].

There are modifications of the MAO process, in which treatment is carried out not in aqueous electrolyte solutions, but in molten salts [74]. One such type of surface treatment of valve metals is plasma electrolytic fluorination. The coating process is also accompanied by microdischarges and is characterized by a forming curve of a form standard for MAO. However, the synthesized coatings consist of metal fluorides and they are distinguished by high chemical purity. Fluoride coatings on aluminum are in demand in optics due to their low refractive index, in the lithium-ion batteries production [74,75]. Magnesium fluoride coatings are promising in the field of medicine due to their high biocompatibility [76]. When using special electrolyte compositions, coatings can be obtained at room temperature,



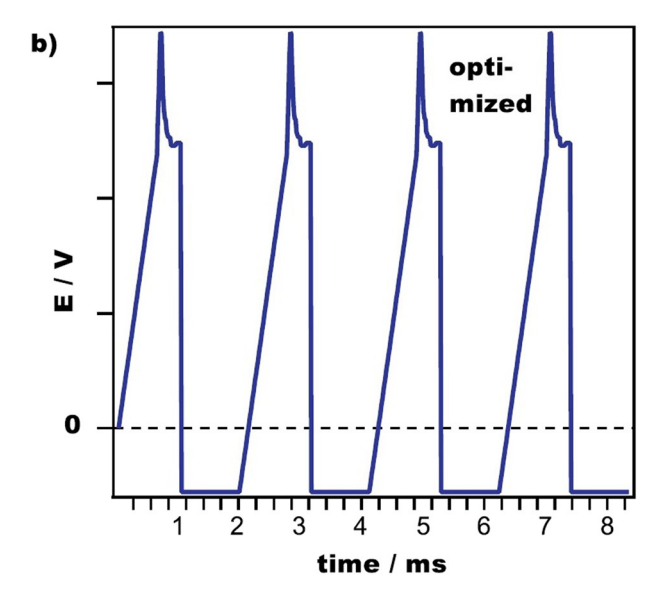


**Figure 2:** Applied waveforms used for the PEO process: (a) Original ultraceramic bipolar-pulsed process and (b) optimized ultraceramic bipolar-pulsed process with additional on-top signal [71].

which makes it possible to simplify the design and increase the efficiency of process equipment.

There are simpler modifications of the MAO process that also impact the properties of the obtained layers such as ultrasound-assisted MAO (UMAO) and heat treatment. The UMAO method makes it possible to increase the corrosion resistance of coatings by reducing the pore diameter, thickening the barrier and working layers and increasing the uniformity of the coating in thickness [77]. In the context of medical application, coatings obtained by UMAO of Ti–Cu alloy demonstrate high hydrophilicity and antibacterial properties [78]. Another way to obtain a continuous compact coating structure is MAO with subsequent heat treatment, which reduces the coating porosity by filling the pores with oxide, as well as healing cracks due to phase transitions of crystalline oxides during annealing at high temperature [59]. At the same time, the hardness and the coatings' wear resistance increase [79].

It should be noted that the described modifications basically retain the characteristic features inherent in the original technology of MAO, and, therefore, all its shortcomings. Thus, the improvement of the MAO process can lead to significant progress in a number of "related" technological processes.

### 3 Mechanism of MAO coating formation

At the present stage, a complete understanding of the mechanism of MAO coating formation has not yet been achieved. The available theoretical information is continuously supplemented, refined, and concretized, up to a complete revision of the obtained results and the emergence of alternative models and hypotheses. The following general ideas about the mechanism of MAO coating formation are valid for aluminum, magnesium, titanium, and their alloys [1–3].

It is known that the MAO process has a pronounced staging [80]. The stage of anodization, spark, microarc, and arc discharges are distinguished [81]. At the stage of anodization, microdischarges do not occur; at the stage of spark discharges, many small sparks are observed that quickly move over the sample surface. The stage of microarc discharges is characterized by the appearance of large but slowly moving discharges [82]. At the stage of arc discharges, several high-power microdischarges burn on the sample surface, which leads to the destruction of coatings [83]. The stages of the MAO process are clearly seen on the forming curve (dependence of the maximum voltage in the galvanic cell on time) (Figure 3).

At the stage of anodization, electrochemical oxidation of the anode occurs [1]. In this case, three sections can be distinguished on the forming curve (Figure 4). In the first section (from 0 to 5 s), a dense barrier oxide layer grows, the next 5 s correspond to the luminescence region, where the porous coating layer grows; a period of time from 10 to 15 s corresponds to the section of the breakdown of the anode oxide film; then the stage of spark discharge comes. The barrier and porous coating layers are composed of amorphous oxides. Thus, before breakdown, an MAO coating uniform in thickness is formed by the mechanism of ion migration. As the oxide layer grows, its temperature rises, which can contribute to the appearance of crystalline phases

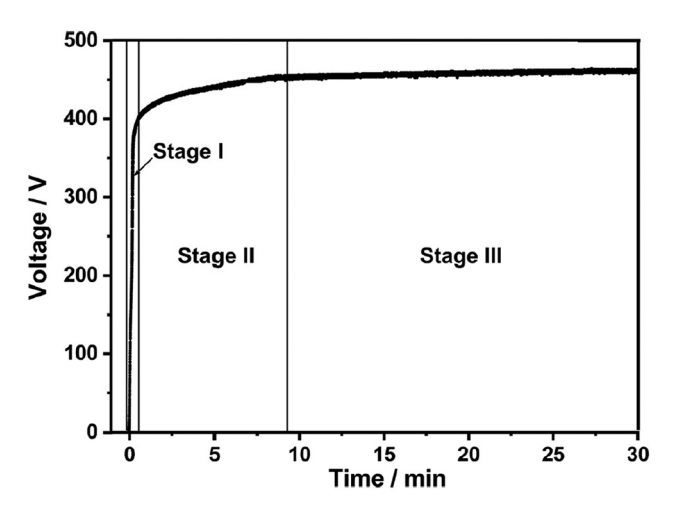


**Figure 3:** The curve of cell voltage *vs* time at the first 30 min of the PEO process. The cell voltages are the peak values of the potential pulses [84]. Region I on the graph corresponds to the anodization stage, region II corresponds to the stage of spark discharges, and region III corresponds to the stage of microarc discharges.

in the coating composition, as well as the intensification of the dissolution process of the coating surface with electrolyte, which can serve as prerequisites for subsequent dielectric breakdown [84]. In the breakdown area, sudden dielectric breakdown of the coating occurs, which leads to the ignition of microdischarges.

At present, there are three versions of the mechanism of occurrence and combustion of a single microdischarge. The first one assumes that the initial dielectric breakdown occurs in the barrier layer at the bottom of the pores, since the resistance of the oxide barrier layer (and the voltage drop on it) is higher than the resistance of the metal sample and electrolyte. At the moment of breakdown, energy is released in the form of Joule heat, as a result of which the electrolyte boils up and a vapor-gas bubble is formed, in which a gas discharge is ignited. In this case, plasma-

chemical reactions occur in the discharge channel, during which base metal and electrolyte oxides, which are part of the coating are formed. Under the action of high plasma temperature, the coating areas adjacent to the discharge channel are melted. When heated, the gas-vapor bubble expands and rushes to the pore mouth. Having gone beyond the pore, the bubble expands, and the micro-discharge goes out. Further, the bubble collapses, the electrolyte vapors condense, and a low-pressure zone forms in the pore, as a result of which a part of the molten oxide is ejected onto the coating surface and rapidly solidifies, forming an amorphous phase [28,49]. Finally, the pore is filled with electrolyte. As a result of these processes, the coating acquires a characteristic crater-like structure [28].

According to the second version, the following processes take place at the moment of breakdown. Under the action of a microdischarge, the coating at the bottom of the pore evaporates and thermal stress arises in this place, which leads to the curvature of the bottom and walls of the pore. Further, when the thermally activated areas come in contact with the electrolyte, a new oxide layer rapidly forms in the pore. In contrast to the first version, the considered mechanism assumes that dielectric breakdown contributes little to coating thickening [84].

The third version assumes that microdischarges occur in the places of structural defects, where the electric field is localized due to charge accumulation, and depending on the type of defect, the process of microdischarge generation proceeds differently (Figure 5). On the ledges of the coating, an accumulation of positive charges occurs; when the sum of the voltage from the accumulated charge and the applied voltage reaches a certain value, dielectric breakdown takes place and sparks occur. In this case, energy is expended on expansion of the discharge channel and thermal work (formation of a gas-vapor bubble under the action of Joule heat, heating of the coating areas

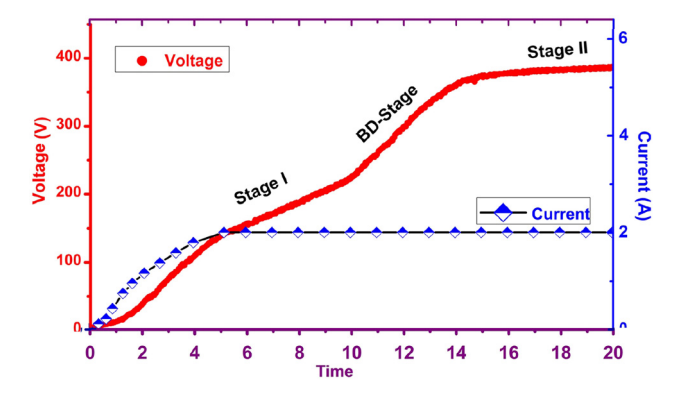


**Figure 4:** The curves of cell voltage (red line) *vs* time and current (blue line-symbol plot) *vs* time [84]. BD-stage – breakdown section.

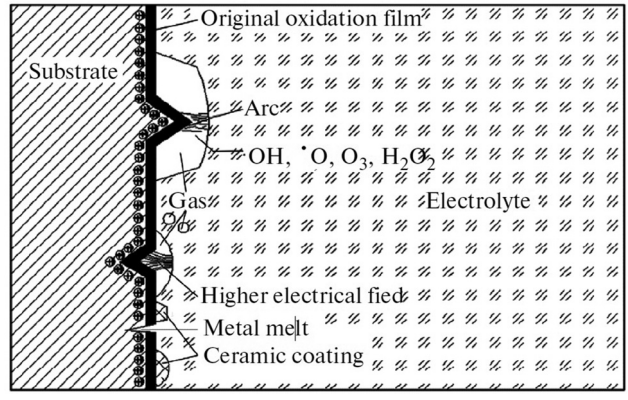


Figure 5: Schematic of the surface process during MAO treatment [31].

adjacent to the discharge channel). In general, the emergence and burning of microdischarges on the coating protrusions occur according to the mechanism described in the first version.

On flat areas of the coating, the probability of microdischarges occurring is negligibly small compared to areas of protrusions due to insufficient energy for inelastic collisions of gas molecules. In the process of coating growth, new protrusions, on which microdischarges appear faster and they are constantly formed. Thus, only electrochemical processes take place on the flat areas of the coating.

In areas of recesses, due to their special shape, the electric field strength increases significantly. It leads to rapid ionization and the appearance of a plasma discharge. In contrast to the protrusion sections, the process proceeds under adiabatic conditions (without heat release). In this case, the plasma temperature in the region of plasma-chemical reactions reaches 8,000 K, and in the adjacent electrolyte – about 300 K, and the temperature drop occurs quite sharply. With a rapid increase in pressure, an explosive expansion of the gas-vapor bubble take place, resulting in the formation of a crater-like structure of the coating [31].

At the stage of spark discharges, the microdischarges functioning mechanism is also ambiguous. According to Hussein *et al.* [83], the stage of spark discharges is characterized by type B microdischarges (Figure 6), which occurs as a result of a thorough dielectric breakdown of the coating, which turns into a thermal one. In this case, the growth of the coating occurs due to melting of the discharge channel walls and plasma reactions involving atoms and ions of the melt and electrolyte. On the contrary, it was shown by Zhu

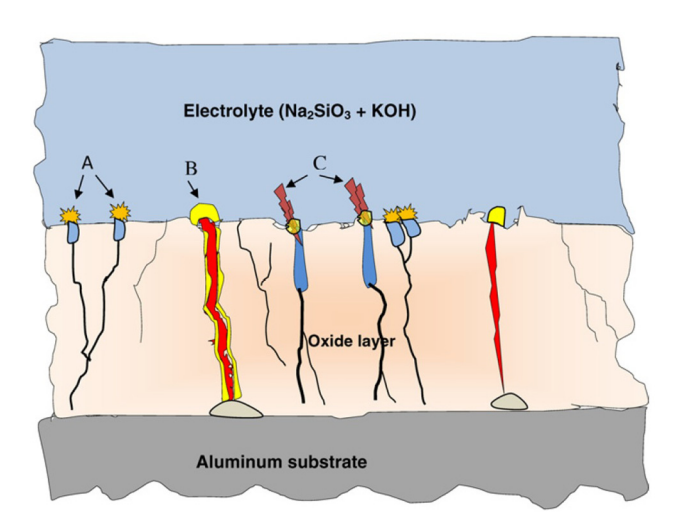


**Figure 6:** Schematic diagram of the discharge models for the PEO process for an Al sample [83].

et al. [84] that dielectric breakdowns of the coating do not occur at the stage of spark discharges. Microdischarges in this case represent a gas plasma burning on the sample surface, while in depth, the coating thickness grows due to ion migration [84]. A characteristic phenomenon at the stage of spark discharges is the so-called "wandering microdischarges," the appearance of which is associated with the thermally activated growth of neighboring coating areas, as a result of which the probability of dielectric breakdown and ignition of microdischarges increases in these places [83].

At the stage of microarc discharges, the coating growth occurs due to ion migration in the barrier layer, while powerful microarc discharges exist in the outer layer pores [84], under the influence of which the temperature of the inner layer of the coating increases, which promotes phase transitions of amorphous oxides into crystalline ones [55]. When the local heating is removed, micrometer-sized aluminum oxide grains form in the regions adjacent to the microdischarge channel, which is accompanied by cracking [85]. At this stage, the formed coating has a classical three-layer structure (barrier layer, working layer, and outer porous layer) [84].

As the treatment time increases, fewer "weak spots" remain on the coating surface [86], which leads to the occurrence of arc discharges. Due to the high power, each arc discharge burns through the coating all the way to the base metal, causing the next arc discharge to occur in the same place. Thus, the transition to the stage of arc discharges is undesirable due to the destruction of the coating.

The stages of microarc and arc discharges are characterized by type A and C microdischarges (Figure 6), which are gas discharges that burn in the micropores of the coating and arise due to a relatively weak dielectric breakdown of the barrier layer at the bottom of the pores. The difference between these types of discharge lies in their localization: Type A microdischarges burn in shallow pores near the coating surface, while type C microdischarges burn in deep micropores or crack under the coating surface. In addition, high-intensity type B microdischarges may be present at the stage of arc discharges [83].

The composition and temperature of microdischarge plasma at different stages of the MAO process also differ. The base metal ions predominate in the spark discharge plasma; in the plasma of microarc discharges, both atoms of the base metal and electrolyte components are ionized; in the spectrum of arc discharges, individual peaks of high intensity are observed [83]. At the initial stages of the MAO process, when the surface density of microdischarges is high, the plasma electron temperature reaches 8,000 K. At subsequent stages, the plasma temperature decreases to 3,000 K (Figure 7) [87].

8 — Ekaterina Pecherskaya *et al.* DE GRUYTER

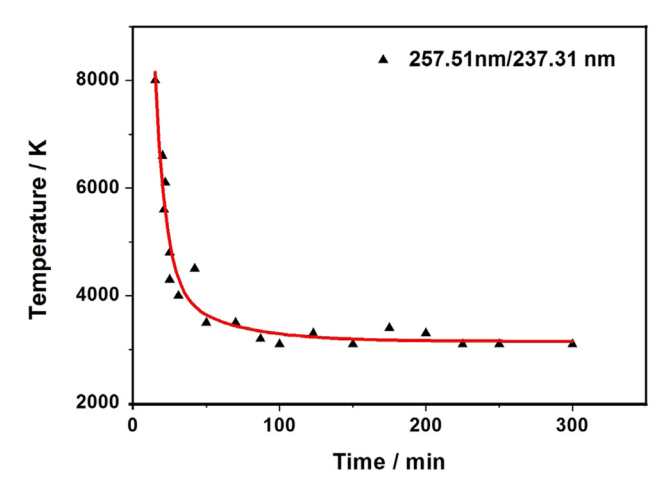


**Figure 7:** Time dependence of plasma temperature determined by means of intensity ratios of Al I spectral lines at 237.31 and 257.51 nm [87].

The mechanism of transition between the stages of microdischarges in the MAO process is also the subject of scientific discussions. According to one version, the difference between the stages lies in the change in the surface discharge type, while the growth of the coating thickness at all three stages of the MAO process occurs in the same way (through ion migration) [84]. According to another version, the mechanism of microdischarge functioning for all stages of the MAO process remains unchanged. In this case, a change in color, an increase in size, power, and a decrease in the number of microdischarges over time is associated with an increase in the thickness and the resistance of the coating, as a result of which the number of "weak points" in which dielectric breakdown is possible decreases [49]. The validity of this statement is confirmed by the results of previous studies [6,71,86,88].

Much attention is paid to the study of the single microdischarge characteristics. At the moment, it is known that with MAO at a sinusoidal current with a frequency of 50 Hz, the instantaneous peak power of a single microdischarge lies in the range of 6–20 W, and the duration of a single microdischarge in the cascade is 30–50  $\mu$ s [89]. For the pulsed MAO mode, the current of a single microdischarge is 47.4 mA, which corresponds to a current density of 47.4 kA·m<sup>-2</sup>, the microdischarge diameter ranges from 8 to 100  $\mu$ m, and the discharge channel diameter is several  $\mu$ m [90]. In this case, the brightness of a single microdischarge is determined by the current strength in the pulse (Figure 8) [89].

The distribution of microdischarges over the sample surface depends on the localization of defects in the structure of the initial alloy and the formed coating. It is known that areas of "weak points" in which dielectric breakdown

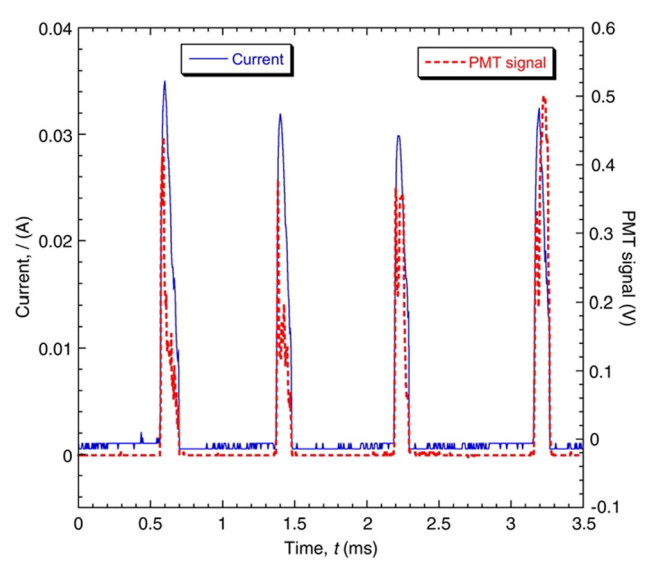


**Figure 8:** Typical data for a sequence of current pulses, and for the associated light emission, obtained from a photomultiplier tube (PMT signal) [89].

occurs, as well as pores that form as a result of microdischarges, are randomly distributed over the coating surface [49,84,91]. It makes it possible to apply statistical methods for the mathematical description of the porous coating formation. For example, from the graphs in Figures 9 and 10, we can conclude that the largest number of observed microdischarges are short-lived microdischarges of small size [6].

Thus, at present, there are fundamental problems concerning the mechanism of MAO coating formation. In particular, there are discrepancies in the interpretation of physical phenomena associated with the dielectric breakdown of the coating, as well as the microdischarge occurrence and combustion. These ambiguities can lead to errors in modeling the synthesis of microarc oxide coatings.

## 4 Influence of heterogeneous factors on the properties of MAO coatings

The properties of MAO coatings are affected by a large number of heterogeneous factors. These can be the electrical parameters of the coating process (current density, amplitude, frequency, duty cycle and polarity of high-voltage pulses, the anode and cathode current ratio), the parameters of the original sample (the workpiece shape, alloy composition, surface roughness), electrolyte parameters (temperature, turbidity, concentration of components and

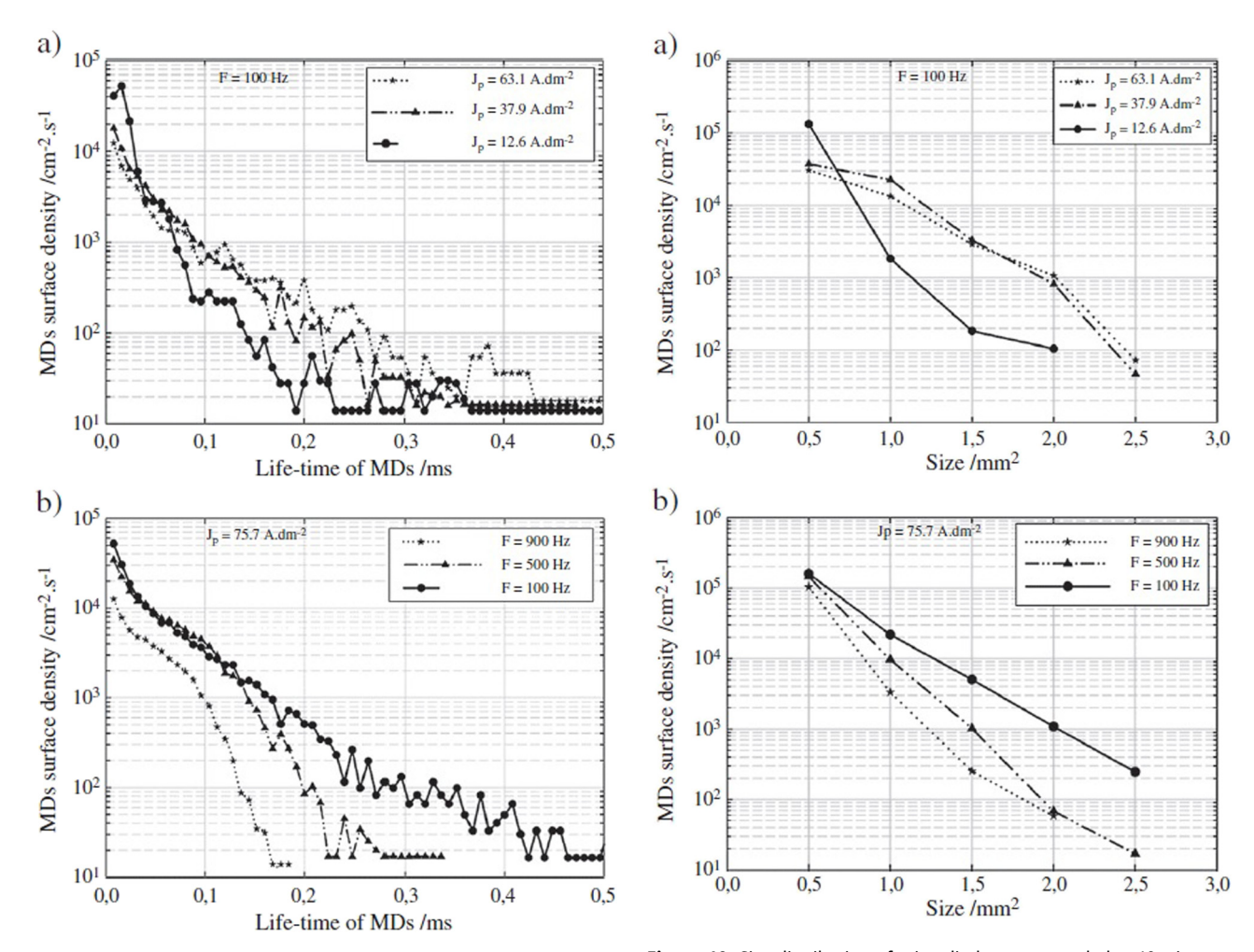


**Figure 9:** Lifetime distribution of microdischarges recorded at 10 min processing time (before "soft" sparking regime) for various (a) current densities  $J_p$  (for Al2214 alloy sample processed with F = 100 Hz) and (b) current pulse frequencies F (for Al1050 alloy sample processed with  $J_p = 75.7 \,\text{A}\cdot\text{dm}^{-2}$ ) [6].

**Figure 10:** Size distribution of microdischarges recorded at 10 min processing time (before "soft" sparking regime) for various (a) current densities  $J_{\rm p}$  (for Al2214 alloy sample processed with F = 100 Hz) and (b) current pulse frequencies F (for Al1050 alloy sample processed with  $J_{\rm p}$  = 75.7 A·dm<sup>-2</sup>) [6].

"production"), processing time, *etc.* The study of these influence regularities, which is an important scientific task, since for different applications, the target properties of the coating and, accordingly, the modes of their formation can differ significantly. For a scientifically based selection of optimal technological parameters for any application, the relationship between the influencing factors and the MAO coatings properties is currently being studied. The results of these studies are reviewed below.

### 4.1 Influence of sample material and shape

Depending on the initial alloy composition, there are specific features of the mechanism of the MAO coating formation [92], since in the MAO process, in addition to the main

alloy component, alloying components also participate in the coating formation [93]. Thus, for the MAO of aluminum alloys, an increase in the duration of the anodizing stage is observed compared with the MAO of pure aluminum at a constant breakdown voltage of the oxide layer (Figure 11), which is due to the introduction of non-valve metal atoms into the coating, which are present in the initial alloy [94]. A similar feature is typical for titanium alloys [95]. In the case of Al-Zn-Mg-Cu alloys, *e.g.*, 7050, the presence of zinc impurities in the initial alloy inhibits the formation of  $\alpha$ -Al<sub>2</sub>O<sub>3</sub>, which reduces microhardness, but increases the coating thickness [96]. It is also known that in Cu-containing aluminum alloys, mainly  $\alpha$ -Al<sub>2</sub>O<sub>3</sub> is formed, whereas in Mg-containing aluminum alloys,  $\gamma$ -Al<sub>2</sub>O<sub>3</sub> predominates, which indicates a lower wear resistance of the latter [97].

For magnesium alloys, the effect of the phase composition on the MAO process, internal structure, and MAO

10 — Ekaterina Pecherskaya et al. DE GRUYTER

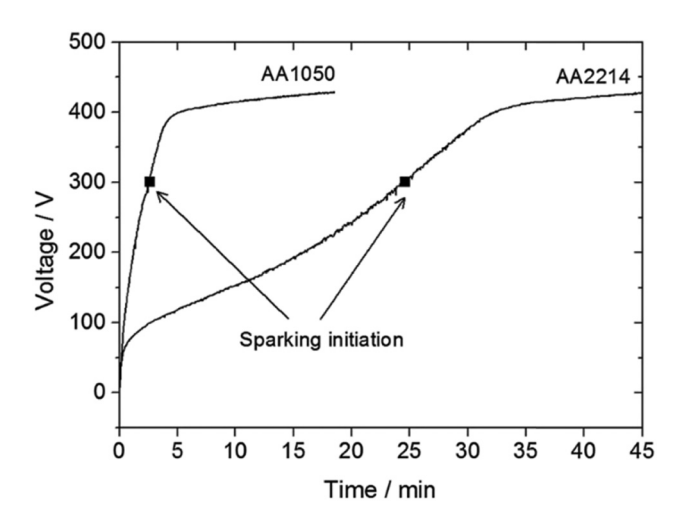


**Figure 11:** Forming curves of MAO process for different aluminum alloys: AA1050 (Si 0.25 wt%, Fe 0–0.4 wt%, Cu 0.05 wt%, Mn 0.05 wt%, Mg 0.05 wt%, Zn 0.05 wt%, Ti 0.05 wt%, Al > 99 wt%) and AA2214 (Cu 3.9–5.0 wt%, Si 0.5–1.2 wt%, Mn 0.4–1.2 wt%, Fe 0.3 wt%, Mg 0.2–0.8 wt%, Zn 0.25 wt%, Cr 0.1 wt%, Ti 0.15 wt%, rest of Al) [94].

coating properties manifests itself differently [93]. In particular, for magnesium alloys, depending on the alloying elements, the formation of a barrier layer of coating occurs in different ways [98,99]. Thus, the growth of the barrier layer of the MAO coating on the AZ91 alloy occurs first on a matrix of  $\alpha$ -Mg, and then passes to the  $\beta$ -phase (Mg<sub>17</sub>Al<sub>12</sub>), while on the WE43 alloy, on the contrary, the barrier layer is formed first on the  $\beta$ -phase (Mg<sub>14</sub>Nd<sub>2</sub>Y), and then on  $\alpha$ -Mg, that is due to the different reactivity of the  $\beta$ -phases

in these alloys [57]. At the same time, the coating growth rate is higher for the  $\alpha$ -phase in the AZ91D alloy, and the coating in the  $\beta$ -phase is formed due to the lateral growth of the oxide in the  $\alpha$ -phase [100]. The increase in the coating growth rate on the AZ91D alloy compared with pure magnesium is due to the presence of Al and Zn in the alloy structure [101].

The structure and properties of the formed coatings on magnesium alloys depend on the alloying elements in the initial one. For example, MAO coatings on the AZ31 magnesium alloy are characterized by the presence of spherical microvoids and branched pores, while MAO coatings on the AZ91 alloy contain a large number of vertical pores (Figure 12), due to which the electric strength of the latter decreases, and the thickness and surface roughness increase. This is due to the presence of intermetallic compounds in the AZ91 alloy [55]. MAO coatings of magnesium alloys containing copper or silicon are characterized by a high degree of unevenness, which increases with an increase in the content of these alloying elements [100].

The ratio of  $\alpha$  and  $\beta$  phases in the substrate material also affects the properties of MAO coatings [35]. So, if the  $\alpha$ -phase prevails in the Mg–Li alloy, the coating consisting mainly of MgO has the greatest thickness, high porosity, and roughness [102]. If the Mg–Li alloy contains mainly the  $\alpha + \beta$  phase, a denser and more uniform coating is formed, which practically has no pores and microcracks [35]. In the AZ91 alloy, the presence of the  $\beta$ -phase leads to the formation of defects in the structure of coatings and deterioration of their corrosion resistance [98].

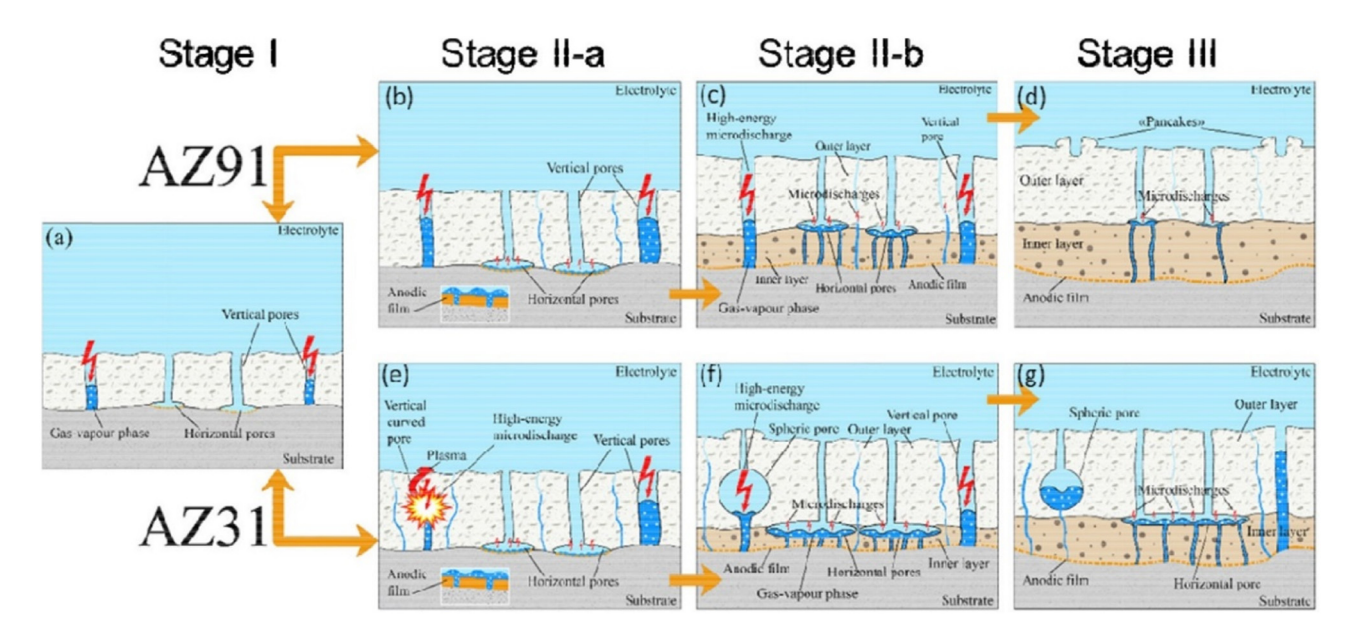


**Figure 12:** Mechanisms and differences of coating formation via ignition of various types of micro discharges during MAO process of AZ31 and AZ91 magnesium alloys in alkaline phosphate-aluminate electrolyte [55]. (a) shows the ignition of anodic plasma micro-discharges in vertical pores for AZ31 and AZ91 alloys. (b, c) shows a very early (Stage II-a) and a later moment (Stage II-b) during MAO processing of AZ91. (e, f) shows the same for AZ31. (d, q) shows the final stage of the MAO processing of AZ31 and AZ91 alloys respectively.

For titanium alloys, the dependence of the structure and properties of coatings on alloying elements and the phase composition of the initial alloy is also traced. For example, the alloying components of titanium alloys in most cases lead to an increase in the MAO coating porosity [46,103,104]; however, the coating structure varies in different ways. For example, an increase in the Ta concentration in the Ti-25Nb-xTa alloy leads to an increase in the thickness and porosity of the coating and a decrease in the pore diameter, which reduces the hardness and modulus of elasticity, but increases the hydrophilicity of the surface [103]. Coatings on the β-Ti<sub>45</sub>Nb alloy are characterized by a lower pore density, but larger diameter, as well as increased roughness compared to the α-titanium alloy [104]. The same is true for  $\alpha/\beta$  alloys, except for the pore diameter, which corresponds to the pore diameter of the MAO coating of a αtitanium alloy [104]. MAO coatings on Ti-18Zr-15Nb alloy have a large thickness, roughness, and porosity due to high values of the diffusion coefficient, and are characterized by increased corrosion resistance [46]. With an increase in the aluminum content in the titanium alloy, the morphology of the coatings also changes: under the action of "wandering microdischarges," a transition from a craterlike surface structure to a crust-like one is observed [105].

The composition of the initial alloy affects the breakdown voltage of the MAO coatings (Table 2), since the growth rate and chemical composition of the oxide depend on it, and therefore its thickness, dielectric constant [119], and melting point [118]. In the case of magnesium alloys, with an increase in the Al content, the breakdown voltage and the microdischarges power increase, which leads to an increase in the coating roughness [120]. With the MAO of Mg-Li alloys, compared with the MAO of pure magnesium. there is a decrease in the breakdown voltage from 150 to 110 V (Figure 13) [102], and the lowest breakdown voltage is characterized by the MAO coating on an alloy in which the α phase prevails, compared with coatings of alloys containing  $\beta$ - and  $\alpha + \beta$  phases [35].

For titanium alloys, similar to magnesium alloys, with an increase in the aluminum content in the alloy, the breakdown voltage of the coating increases, and this dependence is linear (Figure 14) [1,105]. In this case, the increment in the breakdown voltage caused by the increment in the aluminum content in the alloy under study compared to the alloy without aluminum at the stage of microarc discharges is practically independent of the treatment time [59]. The change in the breakdown voltage is associated with a change in the solubility of the molten coating material in the presence of aluminum oxide in its composition. Also, for titanium alloys, depending on the phase composition (during the transition of the  $\alpha \rightarrow (\alpha + \beta) \rightarrow \beta$  phase), the breakdown voltage and the growth rate of the MAO coating increase at the initial and final sections of the forming curve [104]. This is probably due to a change in the dielectric properties of MAO coatings [104]. So, e.g., with the MAO of the Ti-18Zr-15Nb alloy, the alloying components lead to a decrease in current density after the anodizing stage by three times at constant forming voltage compared with the MAO of pure titanium, which indicates a higher resistance of the MAO coating on the Ti-18Zr-15Nb alloy [46]. At the same time, the MAO coating on pure titanium consists of TiO2, and on the Ti-18Zr-15Nb alloy, it consists of TiO2 oxides (anatase and rutile), Nb2O5 and ZrO<sub>2</sub> [46]. Thus, an increase in the resistance of the MAO coating may be due to defects associated with the presence of oxides of other metals in the coating [46].

In addition to the composition of the initial alloy, the breakdown voltage is also influenced by the electrical parameters of the MAO process [121,122], the composition [123], and the temperature of electrolyte [124].

It should be noted that the same allotropic oxide modification can significantly change the properties of MAO coatings on different alloys [125]. Thus, in contrast to aluminum and titanium alloys, a high content of crystalline aluminum oxides in a MAO coating on a magnesium alloy AZ63 does not improve the protective properties of the coating (microhardness and corrosion resistance), but, on the contrary, leads to an increase in the number of defects [49].

Also, the properties of coatings can be influenced by the shape of the coated products [126]. Thus, during the formation of MAO coatings on titanium fiber, a local thickening of the coating from the side of the substrate, followed by the formation of cracks, which reduces the wear resistance and corrosion resistance of the coating is observed. The reason for this phenomenon can be the appearance of intense microarc discharges that burn for a long time on the same surface area and form a local thickening of the coating. In addition, ejections of a large amount of molten oxide onto the sample surface after the extinction of such microdischarges lead to an increase in the coating roughness [127].

### 4.2 Influence of electrical parameters of the process (forming voltage, current density, frequency, and duty cycle)

The MAO electrical and process parameters have a significant influence on the formation and performance characteristics of coatings. For example, the growth rate of MAO coatings increases linearly with the current density and is

Table 2: Breakdown voltage values of MAO coatings of different alloys

Substrate material	Electrolyte	Technological mode	Coating material	Breakdown voltage (V)	Ref.
Aluminum	12.5 g·L <sup>-1</sup> Na <sub>2</sub> SiO <sub>3</sub> , 5 g·L <sup>-1</sup> KOH	Unipolar pulsed mode, current density 0.1 A·cm <sup>-2</sup> , frequency 100 Hz, duty cycle 40%	Al <sub>2</sub> O <sub>3</sub> , SiO <sub>2</sub>	200–250	[84]
A6N01	30 g·L <sup>-1</sup> Na <sub>2</sub> SiO <sub>3</sub> , 2 g·L <sup>-1</sup> KOH	Unipolar pulsed mode, current density 6 A·dm <sup>-2</sup> , frequency 600 Hz, duty cycle 18%	Al <sub>2</sub> O <sub>3</sub>	300-350	[106]
AA1050	KOH (0.033 mol·L <sup>-1</sup> ) and Na <sub>2</sub> SiO <sub>3</sub> (0.05 mol·L <sup>-1</sup> )	Galvanostatic mode, current density 15 mA·cm <sup>-2</sup>	y-Alumina	300	[94]
AA1050	0.01 M NaOH solution	DC unipolar mode, current density 10 A·dm <sup>-2</sup>	Al <sub>2</sub> O <sub>3</sub>	150	[98]
1100	$Na_2SiO_3$ (8 g·L <sup>-1</sup> ) with the addition of KOH to adjust the pH	Pulsed DC mode, current density 0.1 A·cm <sup>-2</sup> , frequency	$Al_2O_3$ , SiO <sub>2</sub>	406	[83]
		2 kHz, duty cycle 80%			
6061	10 g·L <sup>-1</sup> Na <sub>2</sub> SiO <sub>3</sub> , 0.7 g·L <sup>-1</sup> (NaPO <sub>3</sub> ) <sub>6</sub> , 0.1 g·L <sup>-1</sup> NaOH, 1 g·L <sup>-1</sup> NaF. 3 ml·L <sup>-1</sup> CcH <sub>8</sub> O <sub>3</sub>	Unipolar pulsed mode, current density $3\mathrm{A}\cdot\mathrm{dm^{-2}},$ freguency 100 Hz	$\gamma$ -Al <sub>2</sub> O <sub>3</sub> , SiO <sub>2</sub>	200–250	[107]
6063	Na <sub>2</sub> SiO <sub>3</sub> (10 g·L <sup>-1</sup> ), NaF (3 g·L <sup>-1</sup> ), Na(PO <sub>3</sub> )6, (2 g·L <sup>-1</sup> ), NaOH (1 g·L <sup>-1</sup> )	Constant voltage mode, anodic current density 2 A·dm <sup>-2</sup> , cathodic current density 1 A·dm <sup>-2</sup> frequency 500 Hz duty	$\gamma$ -Al <sub>2</sub> O <sub>3</sub>	300-320	[108]
		cycle 10%			
AA6082	3-5 g·L <sup>-1</sup> Na <sub>4</sub> P <sub>2</sub> O <sub>7</sub> , 3-5 g·L <sup>-1</sup> Na <sub>2</sub> SiO <sub>3</sub> , 1-2 g·L <sup>-1</sup> KOH	AC sinusoidal mode, frequency 50 Hz, current density 1,500 A·m <sup>-2</sup>	$Al_2O_3$	150–200	[68]
AA2214	KOH (0.033 mol·L <sup>-1</sup> ) and Na <sub>2</sub> SiO <sub>3</sub> (0.05 mol·L <sup>-1</sup> )	Galvanostatic mode, current density 15 mA·cm <sup>-2</sup>	y-alumina	300	[94]
Titanium	7.2 g·L <sup>-1</sup> NaH <sub>2</sub> PO <sub>4</sub> , 15.8 g·L <sup>-1</sup> Ca(CH <sub>3</sub> COO) <sub>2</sub>	Galvanostatic pulsed mode, current density 60 mA·cm <sup>-2</sup> ,	Anatase and rutile	300	[109]
·	· · · · · · · · · · · · · · · · · · ·	rrequency 1,000 Hz, duty cycle 10%	;	;	;
Titanium	10 g·L ' NaAlO <sub>2</sub> , 4 g·L ' KOH	Fulsed DC potentiostatic mode, applied voltage 400 V,	$TiAl_2O_5$ , $\gamma$ - $Al_2O_3$	340	[110]
a-coTi	0.02 M calcium alycerophosphate. 0.15 M calcium acetate	irequency 2,000 Hz, duty cycle 60% Sinusoidal AC mode, frequency 50 Hz, current density	Anatase and rutile	130	[104]
-		20 A·dm <sup>-2</sup>			1
Ti- $xAI$ ( $x = 0, 3, 6, 10, 20$ wt	0.1 M Na <sub>2</sub> B <sub>4</sub> O <sub>7</sub>	Unipolar pulse mode, current density 0.3 A·cm <sup>-2</sup> ,	TiO <sub>2</sub> (anatase and	320-410	[105]
%) alloys		frequency 600 Hz, duty cycle 9%	rutile), B <sub>2</sub> O <sub>3</sub> , Al <sub>2</sub> O <sub>3</sub>		
Ti <sub>6</sub> Al₄V	$Na_2SiO_3\ 20\ g\cdot L^{-1},\ KOH\ 1\ g\cdot L^{-1};\ Na_3PO_4\ 20\ g\cdot L^{-1},\ KOH\ 1\ g\cdot L^{-1}$	Current density 10 A·dm <sup>-2</sup> , duty cycle 10%, frequency	Anatase and rutile	200	[111]
Ti.Al.V	NaAIO. 20 gt -1 and KOH 1 gt -1	Current density 10 4-dm <sup>-2</sup> duty cycle 10% frequency	ALTIO- V-ALO	300	[111]
.6,4		100 Hz	Na <sub>2</sub> Al <sub>2</sub> xO <sub>3x+1</sub>		-
Ti-40Nb	0.1 M NaOH	Galvanostatic anodic mode, current density $0.5\mathrm{A\cdot cm^{-2}}$	TiO <sub>2</sub> (anatase and	125–150	[112]
B-Ti₄sNb	0.02 M calcium alveerophosphate. 0.15 M calcium acetate	Sinusoidal AC mode. frequency 50 Hz. current density	rutile), ( $I_1xND_{1-x}$ ) $O_2$ Anatase	132	[104]
<del>}</del> -		20 A·dm <sup>-2</sup>			·
α/β-Ti <sub>6</sub> Al <sub>7</sub> Nb	0.02 M calcium glycerophosphate, 0.15 M calcium acetate	Sinusoidal AC mode, frequency 50 Hz, current density	Anatase and rutile	140	[104]
R-Ti-r7r40Nh	0.02 M calcium plycerophosphate 0.15 M calcium acetate	Sinusoidal AC mode frequency 50 Hz current density	Ti <sub>2</sub> 7rO <sub>2</sub>	150	[104]
Z., 101.75 € 1.01.75		20 A·dm <sup>-2</sup>	0 1771	2	
Ti <sub>13</sub> Zr <sub>13</sub> Nb	$0.1\mathrm{mol\cdot L^{-1}C_3H_7CaO_6P}$ , and $0.15\mathrm{mol\cdot L^{-1}Ca(CH_3COO)_2}$	Maximum voltage 400 V, current 50 mA		150-200	[113]
Ti–36Nb–3Zr–2Ta		DC PEO process, current density 150 mA·cm $^{-2}$ , limiting cell $$ TiO $_{\!2},$ Nb $_{\!2}$ O $_{\!5}$ voltane 500 V	TiO <sub>2</sub> , Nb <sub>2</sub> O <sub>5</sub>	150–200	[13]
					(Continued)

Table 2: Continued

Substrate material	Electrolyte	Technological mode	Coating material	Breakdown voltage (V)	Ref.
	The composition of the electrolytes was chosen to attain the Ca/P or (Ca + Mg)/P atomic ratios of 1.67 or 2.00, respectively, in each solution				
Magnesium	2 g·L <sup>-1</sup> NaOH, 6 g·L <sup>-1</sup> K <sub>2</sub> ZrF <sub>6</sub> , 5 g·L <sup>-1</sup> NaO <sub>18</sub> P <sub>6</sub> , 3 g·L <sup>-1</sup> NaF	Bipolar pulsed mode, anodic maximum voltage 800 V, cathodic maximum voltage 250 V, anodic current density 4.34·10 <sup>-2</sup> A·cm <sup>-2</sup> , cathodic current density 3.62·10 <sup>-2</sup> A·cm <sup>-2</sup> , frequency 500 Hz, duty cycle 10%	Mgo, t-ZrO <sub>2</sub> , Mg <sub>2</sub> Zr <sub>5</sub> O <sub>12</sub>	300	[114]
AZ31	0.1 M KOH, 0.05 M Na <sub>2</sub> SiO <sub>3</sub>	Current density 50 mA·cm <sup>-2</sup> , frequency 60 Hz	MgO, MgSiO <sub>3</sub>	200–225	[115]
AZ31B	3 g·L <sup>-1</sup> КОН, 10 g·L <sup>-1</sup> Nа <sub>3</sub> PO <sub>4</sub> , 2 g·L <sup>-1</sup> Са(ОН) <sub>2</sub> .	Current density 300 mA·cm <sup>-2</sup> , frequency 1,000 Hz, duty cycle 20, 50, 80%	MgO, $Mg_3(PO_4)_2$ , CaNaPO <sub>4</sub>	450–550	[116]
AZ31B	$6 \text{ a} \cdot \text{L}^{-1} \text{ Na}_2 \text{SiO}_3$ , $2 \text{ a} \cdot \text{L}^{-1} \text{ KF}$ , $2 \text{ a} \cdot \text{L}^{-1} \text{ KOH}$ , 10 mL·L <sup>-1</sup> alveerol	Current density 30 mA·cm <sup>-2</sup>	MgO, Mg,SiO,	250-300	[117]
AZ91	10 g·L <sup>-1</sup> Na <sub>3</sub> PO <sub>4</sub> , 1g·L <sup>-1</sup> KOH	Pulsed bipolar mode, positive current density of	MgO	300	[57]
		$5.0\mathrm{A\cdot dm^{-2}}$ , negative voltage 110 V, frequency 150 Hz, positive pulse 1.0 ms, negative pulse 1.5 ms.			
AZ91D	15 g·L <sup>-1</sup> NaAlO <sub>2</sub> , 1.2 g·L <sup>-1</sup> КОН	The treatments were performed at constant current density (15 mA·cm <sup>-2</sup> ) using a DC power supply of 600 V/	MgO	200–250	[118]
WE43	10 g·L <sup>-1</sup> Nа <sub>3</sub> PО <sub>4</sub> , 1 g·L <sup>-1</sup> КОН	20 A capacity Pulsed bipolar mode, positive current density of 5.0 A·dm <sup>-2</sup> , negative voltage 110 V, frequency 150 Hz, positive pulse 1.0 ms, negative pulse 1.5 ms	MgO	300	[57]

0.15 wt% others, and balance Al (Al-Mg-Si alloy). 6063: 0.2-0.6 wt% Si, 0.35 wt% Fe, 0.1 wt% Cu, 0.1 wt% Mn, 0.45-0.9 wt% Mg, 0.1 wt% Cr, 0.1 wt% Zn, 0.1 wt% Ti, 0.15 wt% others, and balance Al (Al-Mg-Si alloy). 0.5-1.2 wt% Si, 0.7 wt% Fe, 3.9-5 wt% Cu, 0.4-1 wt% Mn, 0.2-0.8 wt% Mg, 0.1 wt% Cr, 0.25 wt% Zn, 0.15 wt% Ti, 0.05 wt% Zr, 0.15 wt% others (Al-Cu-Si aluminum wrought alloy). a-cpTi: commercially pure titanium. Ti-xAl (x = 0, 3, 6, 10, 20 wt%) alloys: 0, 3, 6, 10, 20 wt% Al and balance Ti. Ti<sub>6</sub>A<sub>4</sub>V: 6 at% Al, 4 at% V, and balance Ti (Ti-Al-V alloy). Ti-40Nb: 40 at% Nb, 60 at% Ti(Ti-Nb alloy). B-Ti<sub>45</sub>Nb: 45 at% Nb, 55 at% Ti. (Ti–Nb alloy). α/β-Ti<sub>6</sub>Al<sub>7</sub>Nb: 6 at% Al, 7 at% Nb, and balance Ti (Ti–Al–Nb alloy). β-Ti<sub>3</sub>SZ<sub>10</sub>Nb: 35 at% Zr, 10 at% Nb, and balance Ti (Ti–Zr–Nb alloy). Ti<sub>13</sub>Zr<sub>13</sub>Nb: 13 at% Zr, 13 at% Nb, and balance Ti (Ti-Zr-Nb alloy). Ti-36Nb-3Zr-ZTa: 36 at% Nb, 3 at% Zr, 2 at% Ta, and balance Ti (Ti-Zr-Nb alloy). AZ31: 3.05 wt% Al, 0.82 wt% Zn, 0.4 wt% Mn, 0.02 wt% Si, 0.003 wt% Cu, 0.0012 wt% Ni, 0.0023 wt% Fe, and Alloy compositions from Table 2: A6N01: superpurity aluminum (AI 99,9999%). A41050: 99.5 wt% AI, 0.25 wt% Si, 0.4 wt% Fe, 0.05 wt% Cu, 0.05 wt% Mn, 0.05 wt% Mg, 0.07 wt% Zn, 0.05 wt% Ti, 0.03 wt% others (pure aluminum). 1100: 99 wt% Al (min), 0.12 wt% Cu (pure aluminum). 6061: 0.4-0.8 wt% Si, 0.7 wt% Fe, 0.15-0.4 wt% Cu, 0.15 wt% Mn, 0.8-1.2 wt% Mg, 0.04-0.35 wt% Cr, 0.25 wt% Zn, 0.15 wt% Ti, A6082: 0.7-1.3 wt% Si, 0.5 wt% Fe, 0.1 wt% Cu, 0.4-0.1 wt% Mn, 0.6-1.2 wt% Mg, 0.25 wt% Cr, 0.2 wt% Zn, 0.1 wt% Ti, 0.15 wt% others, and balance Al (Al-Mg-Si alloy). AA2214: 90.8-95 wt% Al, balance Mg (extruded Mg-Al alloy). AZ31B: 97 wt% Mg, 2.5-3.5 wt% Al, 0.6-1.4 wt% Zn, 0.2 wt% Mn, 0.1 wt% Si, 0.05 wt% Cu, 0.04 wt% Ca, 0.005 wt% Fe, 0.005 wt% Fe, 0.005 wt% Ni (extruded Mg-Al alloy). AZ91: 8.8 wt% Al, 0.71 wt% Zn, 0.19 wt% Mn, 0.029 wt% Si, 0.002 wt% Cu, < 0.001 wt% Ni, 0.001 wt% Fe, and balance Mg (high-purity cast Mg-Al alloy). AZ91D: 8.3-9.7 wt% Al, 0.15-0.5 wt% Mn, 0.35-1 wt% Zn, 0.1 wt% Si, 0.03 wt % Cu, 0.005 wt% Fe, 0.002 wt% Ni, others, each max 0.02 wt%, and balance Mg (high-purity cast Mg–Al alloy). WE43: 3.7–4.3 wt% Y, 2.4–4.4 wt% Rare Earths, 0.4 wt% Zr, and balance Mg (high-strength nagnesium alloy)

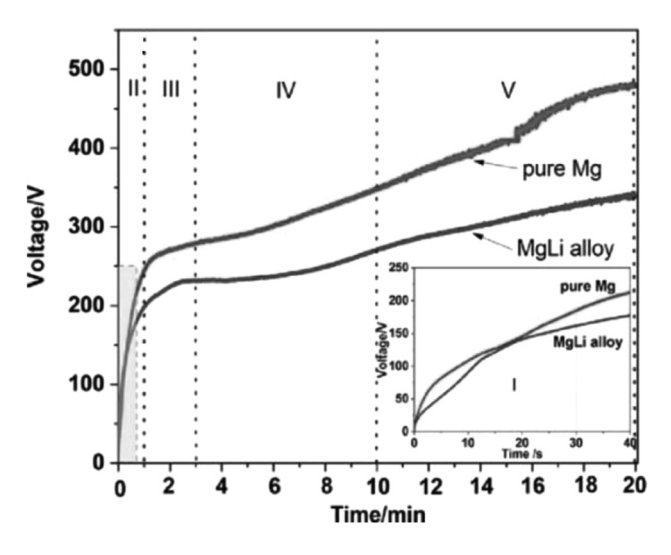


**Figure 13:** Forming curves of the MAO process for pure magnesium and Mq–Li alloy [102].

practically independent of the pulse frequency (a weak direct correlation is possible) (Figure 15) [6]. In this case, the electron and ion current ratio changes depending on the current density. Taking into account that the electrochemical processes responsible for the coating growth are determined by the ion current, while the microplasma processes are determined by the electron current, to ensure stable growth of the coating, it is necessary to maintain a balance between these two currents [123]. The coating breakdown voltage does not depend on the current density [86].

The coatings' porosity is determined by the surface density of microdischarges, which increases with current

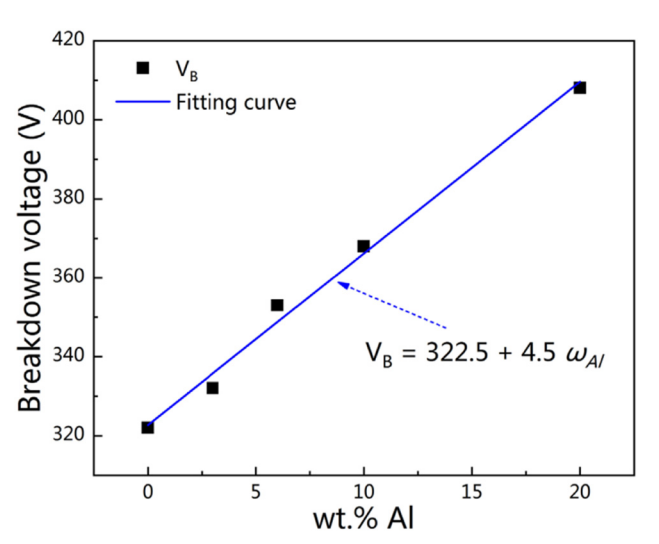
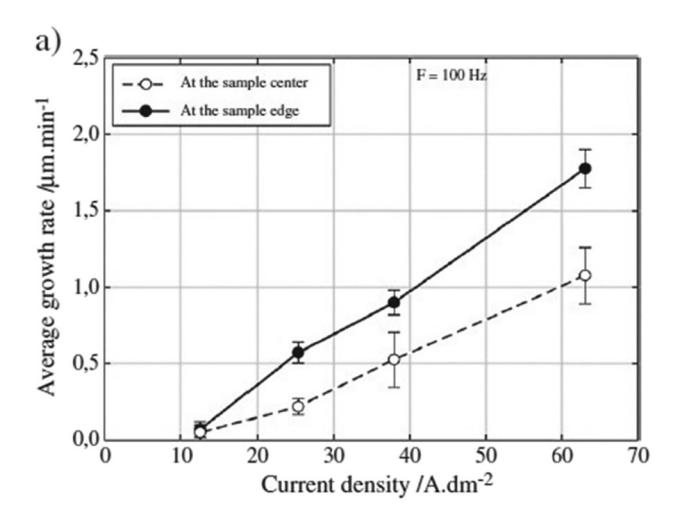


**Figure 14:** Relationship between the breakdown voltage and the Al content ( $\omega_{Al}$ ) in the Ti–xAl alloys during the MAO treatment in 0.1 M Na<sub>2</sub>B<sub>4</sub>O<sub>7</sub> electrolyte [105].

density and decreases with pulse frequency, as shown in Figures 8 and 9 [6]. In this case, the pore size decreases with current density, as well as with an increase in frequency according to an exponential law (Figure 16) [123].

The surface roughness of coatings, as well as porosity, increases with current density and decreases with frequency (Figure 17) [6]. An increase in the coating roughness is also observed with an increase in the applied voltage [127].

With an increase in the duty cycle of the pulses, the content of crystalline oxides, the thickness, and corrosion resistance of the coatings increase, while the breakdown



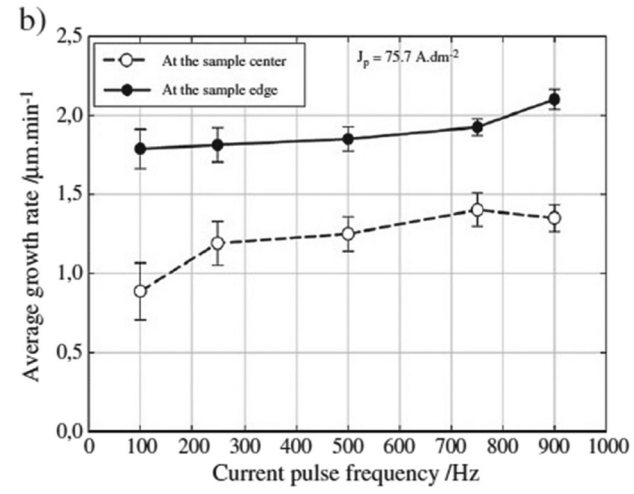


**Figure 15:** Dependence of the average growth rate of the oxide layer at the center and the edge of PEO processed samples on (a) the current density  $J_p$  (for Al2214 alloy sample processed with F = 100 Hz, after 70 min treatment) and (b) the current pulse frequency F (for Al1050 alloy sample processed with  $J_p = 75.7 \text{ A·dm}^{-2}$ , after 40 min treatment) [6].

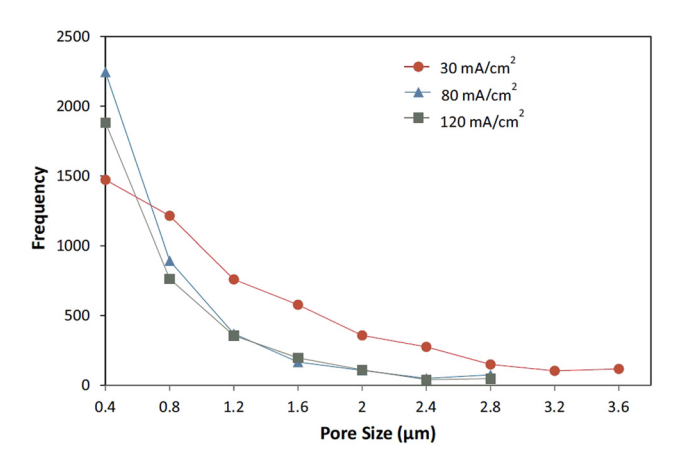


**Figure 16:** Pore size distribution in coatings produced at a current density of 30, 80, and 120 mA·cm<sup>-2</sup> [123].

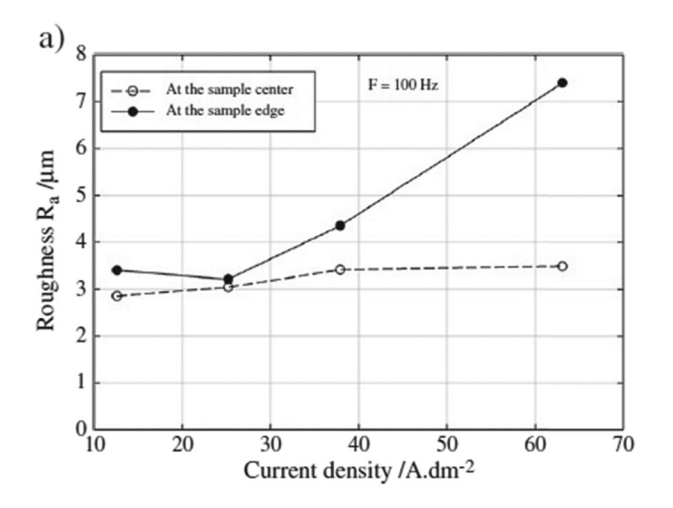
voltage and porosity of the coatings decrease [116]. In this case, if the pulse duration is chosen to be comparable with the microdischarge duration, coatings are formed that have a uniform porosity and a small pore size [121].

The current density and duty cycle of the pulses determine the energy consumption of the MAO process. It was found that the lowest power consumption is achieved at a reduced current density and pulse duty cycle [121]. However, this MAO mode has limitations. At a low duty cycle of the pulses, a short-term increase in the microdischarges power occurs, but the duration of their action is insufficient, which limits the growth rate of the coating thickness. This is due to a change in the transport of ions in the "metal-oxide-electrolyte" system. A high duty cycle accelerates the ions' movement (ions move a greater distance), so the breakdown voltage drops. Thus, in order to effectively obtain MAO

coatings, it is necessary to maintain a duty cycle balance at which the power would be maximum and the duration acceptable for the required coating growth rate [116].

The influence of the electrical parameters of the MAO process on the various properties of the MAO coating layers (working and technological) is manifested as follows:

- With increasing current density, the coating growth rate and the microdischarge power increase, which leads to the formation of thicker coatings [93], an increase in the content of crystalline phases in the working layer, microhardness, and corrosion resistance of the coating [56,128]. The number of microdischarges per unit surface area of the sample also increases, which increases the porosity and roughness of the technological layer [6,123]. Coatings obtained at high current density are characterized by a high degree of defect, which is associated with an increase in the power of microdischarges [93,128]. Thus, due to internal mechanical stresses caused by constant ignition and microdischarges quenching, microcracks occur in the coating [88]. When a microdischarge is ignited, the plasma temperature in the discharge channel and the temperature of the coating adjacent to it increase. When the vapor-gas bubble collapses, the pore is filled with electrolyte and is cooled, a temperature gradient occurs, which leads to rapid recrystallization and the formation of microcracks in the oxide layer [129]. Microcracks can also occur during subsequent heat treatment of coatings if the annealing temperature exceeds 500°C [79].
- With an increase in the pulse duration, the content of crystalline phases in the working layer of the coating also increases, and the porosity of the technological



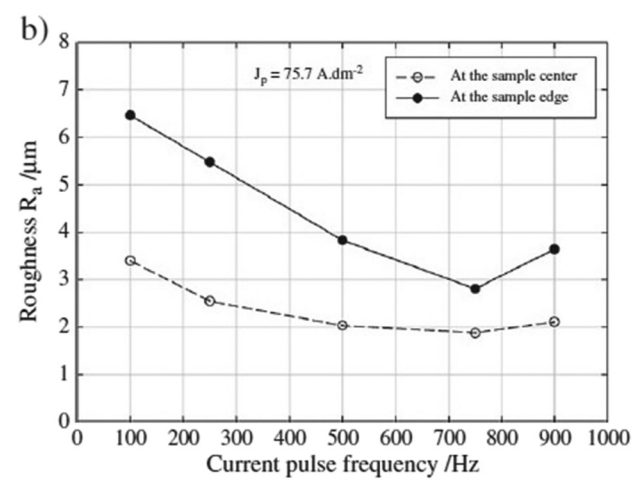


**Figure 17:** Dependence of the roughness of the oxide layer at the center and the edge of PEO processed samples on (a) the current density  $J_p$  (for Al2214 alloy sample processed with F = 100 Hz, after 70 min treatment) and (b) the current pulse frequency F (for Al1050 alloy sample processed with  $J_p = 75.7 \,\text{A} \cdot \text{dm}^{-2}$ , after 40 min treatment) [6].

layer decreases [56,116]. The content of oxides formed by electrolyte components in the technological layer of the coating, *e.g.*, copper oxide, which gives the coating catalytic properties [61,130], as well as mullite [56], depends on the duty cycle of the pulses. Single current pulses of a larger width have a higher energy, which can affect the growth rate, thickness, and pores diameter in the coating [1]. The use of ultrashort current pulses makes it possible to achieve a nanometer-sized grain structure in MAO coatings [131].

- With an increase in the frequency of current pulses, the porosity of the technological coating layer decreases [6], and the oxide content in the coating, thickness, and corrosion resistance increase [93].
- With an increase in forming voltage, an increase in thickness, porosity [1,132], and surface roughness of the coating [127,133] is observed, which is associated with an increase in the power of microdischarges [1]. This reduces the corrosion resistance [93], adhesive strength, thermal conductivity, and crack resistance of MAO coatings under thermal shock [133].
- The influence of voltage polarity is manifested in the difference in the structure and properties of coatings obtained in the anode and anode-cathode modes [1,93,129]. In both these modes, MAO coatings have a classic three-layer structure with a dense working and loose technological layer; however, in coatings obtained in the anode mode, there are a large number of defects at the coating-substrate interface, which indicates low adhesive strength of coatings [129]. In coatings obtained in the anode-cathode mode, the working layer does not contain pores and cracks, which are concentrated in the technological layer of coatings [134]. In addition, the thickness of the working layer of coatings obtained in the anode-cathode mode is higher than in the anode mode [129]. The described differences in the morphology and properties of coatings are explained by the fact that in the anode-cathode mode, the anode pulse is responsible for the course of oxidation reactions, and the cathode pulse has a sintering effect on the formed oxide, which makes the coating more compact and increases corrosion resistance [1,93].
- The ratio of the anode and cathode currents  $I_{\rm A}/I_{\rm C}$  allows us to adjust the ratio of the thickness of the outer and inner coating layer [129]. With a decrease in the ratio of anode and cathode currents  $I_{\rm A}/I_{\rm C}$ , the growth rate of the coating inward (toward the substrate) increases, and the growth rate outward (toward the electrolyte) decreases [134]. At the same time, the thickness of the working layer increases [1,129], and the share of the technological layer in the total thickness of the coating decreases [134]. With a decrease in the ratio of anode and cathode

currents  $I_{\rm A}/I_{\rm C}$ , the hardness of the coatings increases, which is associated with an increase in the content of crystalline oxides in the working layer of the coating [133,134]. The decrease in roughness with a decrease in the ratio of anode and cathode currents is associated with the smoothing of the characteristic "pancake" structure of the technological coating layer [93,129,134].

Due to the variety of pulse modes of MAO processing and a large number of adjustable parameters, the question of the influence of the electrical parameters of the MAO process on the properties of the coatings being formed currently [1], as well as the task of finding optimal technological parameters for obtaining MAO coatings with specified properties remain open [135].

### 4.3 Influence of electric field inhomogeneity

In some works, it is noted that the coating is formed unevenly over the sample surface, as a result of which the coating properties differ somewhat at the center and at the edges of the sample (thickness and roughness are higher at the edges) [6]. As reported in the study by Moga et al. [49], at a coating thickness of 24  $\mu$ m, the deviation of the thickness from the average value is ±12  $\mu$ m. This spatial gradient is more typical for high current densities and low pulse frequencies, and it can be associated with both the uneven distribution of microdischarges over the sample surface [49] and the inhomogeneity of the electric field in the galvanic cell.

Galuza et al. [136], based on the theory outlined in [137], simulated the effect of the distribution of the electric field strength over the sample surface on the heterogeneity of the oxide coating (from the center to the edge of the samples). The simulation results showed that the electric field strength is minimal in the center of the sample and maximal at its edges [136]. The conclusion that along the central line of the sample, the electric field strength increases monotonously from the current input plane to the opposite surface are interesting; in the center of the sample, the field has practically no gradient and is close to homogeneous [136]. Experiments have confirmed that in the early stages of the MAO process, microdischarges are unevenly distributed over the sample area, which causes a more intensive growth of the coating in areas where there are more microdischarges [136,138,139]. Kuznetsov et al. [138] analyzed the influence of the configuration and mutual arrangement of the electrodes and the sample: it was experimentally established that the best results in

uniform distribution of the coating thickness during MAO are provided by the condition of plane-parallel installation of the electrodes relative to the plane of the processed sample. After a short processing time (about 5 min), microdischarges occur mainly along the edges of the sample, which is explained by an increase in the electric field strength due to the presence of an edge effect [6,139].

The reason for the inhomogeneity of the electric field can be, *e.g.*, the complex shape of the coated part, the number and configuration of cathodes, *etc*.

### 4.4 Effect of processing time

Processing time is one of the main influencing factors of the MAO process [135]. The processing time determines the MAO process stage and, consequently, the structure and phase composition of the resulting coatings. Thus, depending on the processing time, both two-layer (consisting of a barrier and porous layers) and three-layer coatings can be formed, having an additional inner, or working, layer [55].

According to the mechanism of MAO coating formation considered earlier, the coatings' thickness increases with the processing time; however, there is ambiguity in the description of this dependence. On the one hand, the coating thickness increases linearly with the treatment time (Figure 18), and the growth rate depends on the electrolyte composition [88]. On the other hand, at the stage of spark discharges, the dependence of the MAO coating

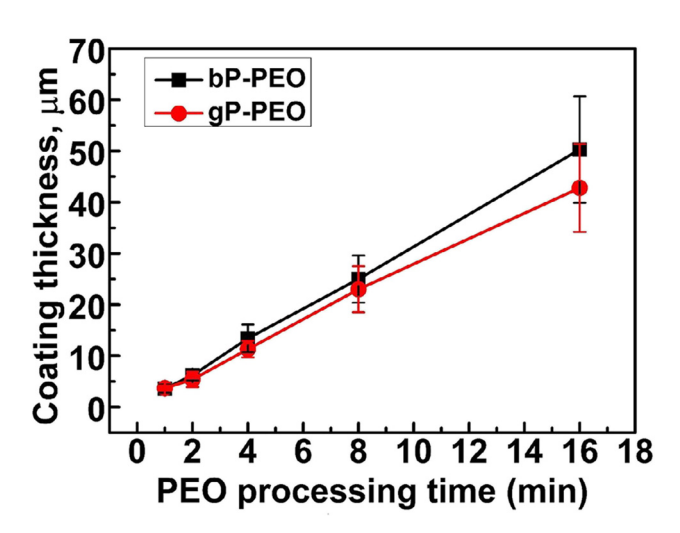


**Figure 18:** Average coating thickness as a function of PEO processing time for both bP-PEO and gP-PEO [88]. The bP-PEO coating was obtained in the base electrolyte,  $Na_3PO_4$  (20  $g \cdot L^{-1}$ ) and KOH (1  $g \cdot L^{-1}$ ). The gP-PEO coating was obtained in the base electrolyte with the addition of glycerol  $C_3H_8O_3$  (250 ml· $L^{-1}$ ).

thickness on the treatment time is described by exponential functions, at the stage of microarc discharges by linear functions (Figure 19), and there is a clear correlation between the empirical constants of the approximating functions at the stage of spark discharges and the concentration of electrolyte components [122]. The linear dependence of the coating thickness on the processing time is valid for a short processing time, after which a fracture is observed. The linear nature of this dependence is obtained as a result of a combination of two mechanisms for the growth of the MAO coating: outward growth (in the direction of the "coating-electrolyte" interface) under the microdischarge action (during splashing and solidification of molten oxide on the coating surface), and inward growth (in the direction of the "coating-substrate" interface) as a result of oxygen diffusion (Figure 20) [140].

With an increase in the treatment time, the coating porosity decreases, and the roughness increases, which is due to an increase in the size of microdischarges and a decrease in their number [49]. The nature of the change in the coating porosity can be estimated knowing the dependence of the surface density of microdischarges on the treatment time. It can be seen that this dependence obeys the double exponential decay law (Figure 21) [6] and is approximated by a straight line on a double logarithmic scale (Figure 22) [86]. This shape of the experimental curves is presumably the result of two different phenomena, which are associated with the features of the dielectric coating breakdown. However, the specific

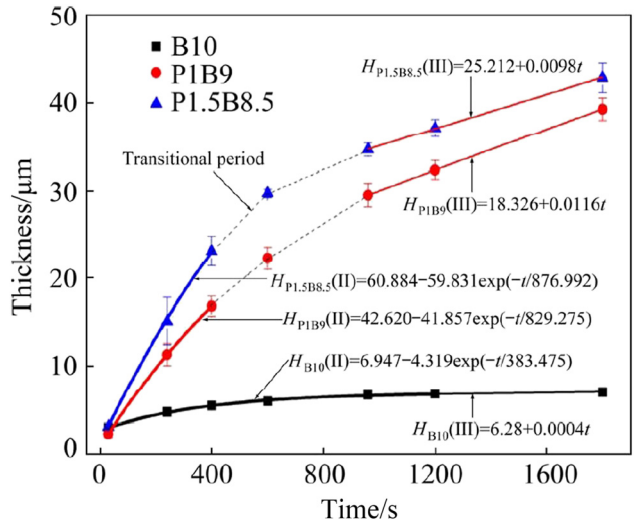


**Figure 19:** Thickness of MAO coating obtained in phosphate-borate electrolytes [122]. Electrolyte composition: for sample B10:  $Na_2B_4O_7$  (0.1 mol· $L^{-1}$ ); for sample P1B9:  $Na_2B_4O_7$  (0.09 mol· $L^{-1}$ ) and  $Na_3PO_4$  (0.01 mol· $L^{-1}$ ); and for sample P1.5B8.5:  $Na_2B_4O_7$  (0.015 mol· $L^{-1}$ ) and  $Na_3PO_4$  (0.085 mol· $L^{-1}$ ).

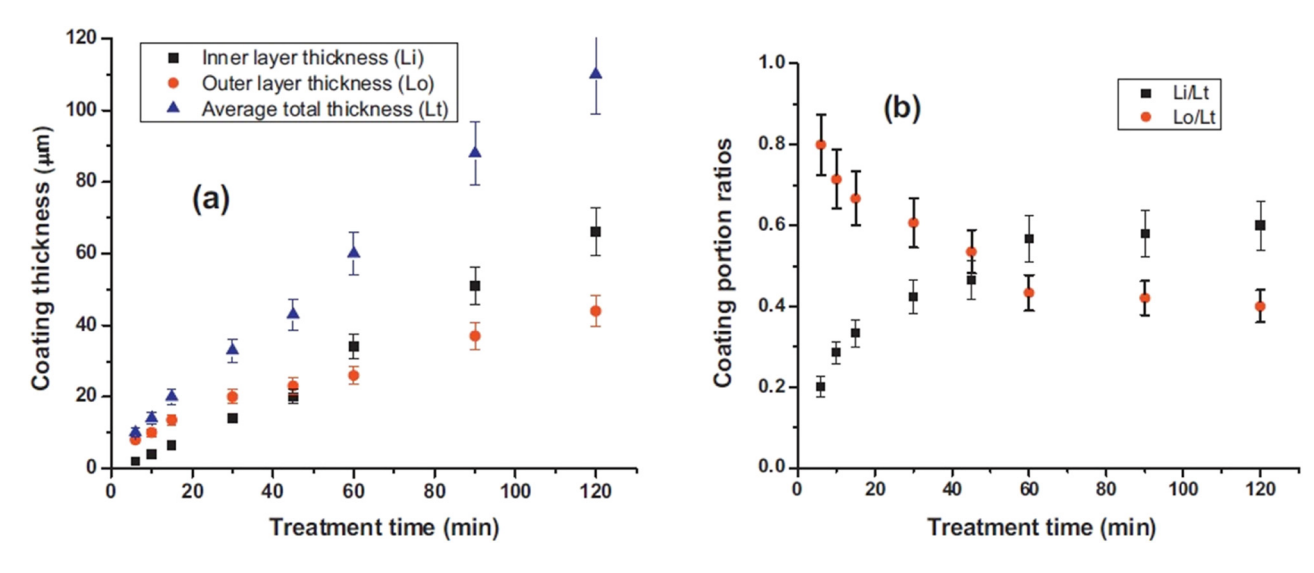
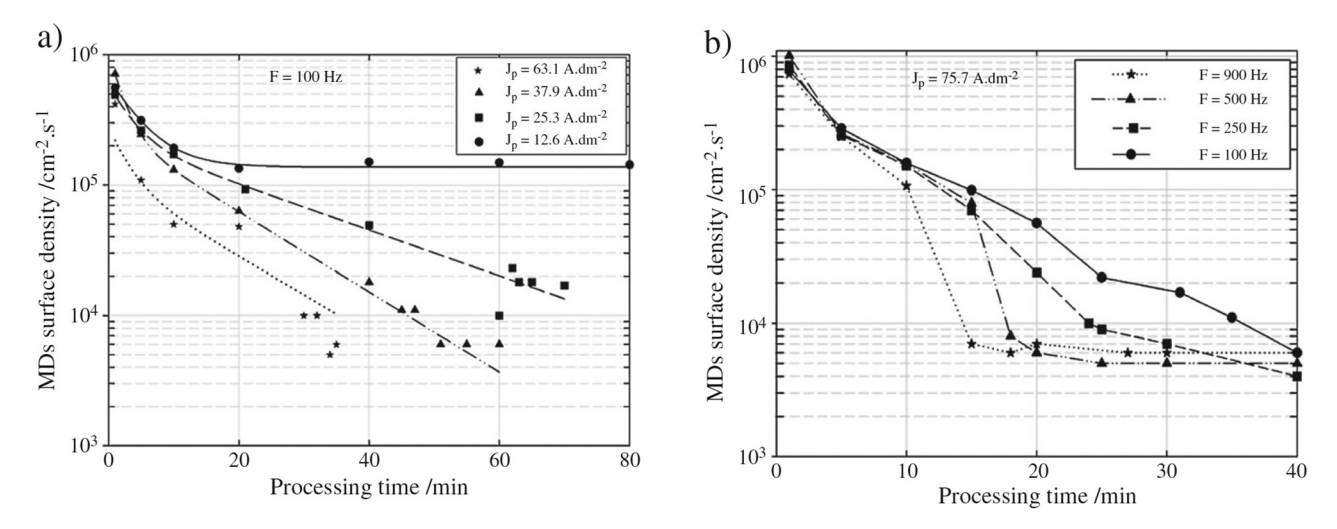


Figure 20: Inward and outward coating portion during PEO coatings (a), ratio of coating portion to the total thickness (b) vs treatment time [140].



**Figure 21:** Microdischarge surface number density as a function of the PEO process time for various (a) current densities  $J_p$  (for Al2214 alloy sample processed with F = 100 Hz) and (b) current pulse frequencies F (for Al1050 alloy sample processed with  $J_p = 75.7 \text{ A} \cdot \text{dm}^{-2}$ ) [6].

mechanisms of these phenomena have not yet been studied [6].

An increase in treatment time also leads to a change in the pore structure: over time, the diameter of the hole in the pore expands, while the diameter of the outer wall of the pore remains constant [84,85,88]. It is known, however, that at the same coating breakdown voltage, the average pore size does not depend on the treatment time [85].

The percentage of crystalline oxides in the coating increases with the treatment time. The percentage of crystalline oxides correlates with the microhardness and corrosion resistance of coatings, which also increase with treatment time. In addition, an increase in microhardness

and corrosion resistance can be associated with a decrease in the coating porosity [49].

### 4.5 Influence of component concentration, pH, and electrolyte conductivity

The mechanism of the electrolyte components concentration influence can be described as follows (using the example of a silicate-alkaline electrolyte). An increase in the NaOH concentration leads to an increase in the electrolyte conductivity, but also intensifies the coating dissolution. The sodium silicate addition to the electrolyte reduces the dissolution rate of

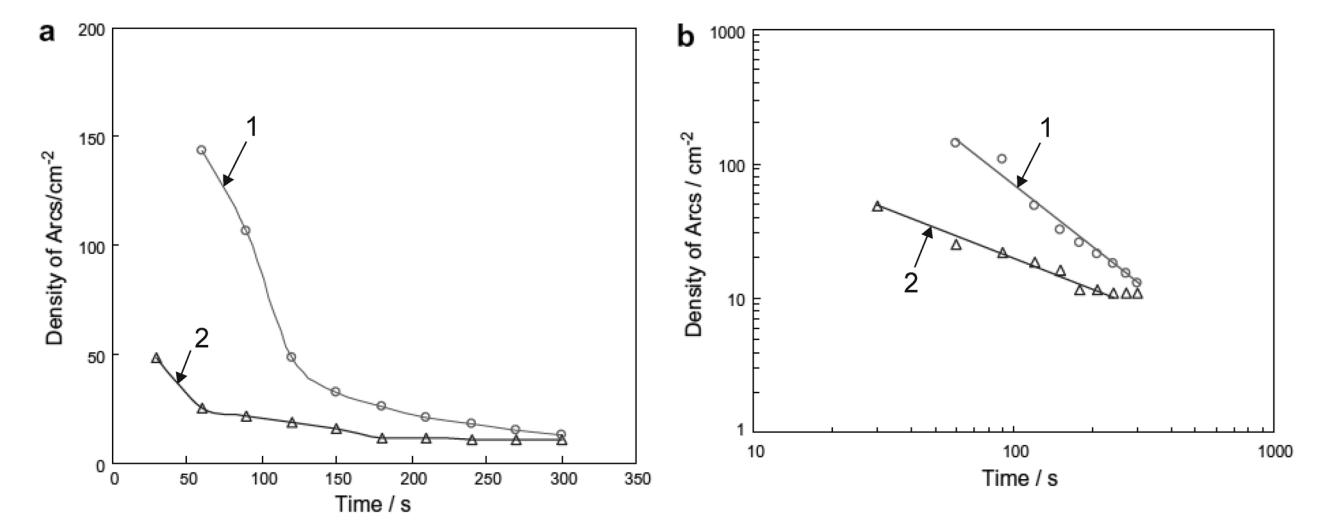


Figure 22: Density of microdischarges versus PEO treatment time of aluminum in  $0.05 \text{ M NaOH} + 10 \text{ g/L Na}_2\text{SiO}_3 \text{ at 5 (curve 1) and } 10 \text{ A} \cdot \text{dm}^{-2} \text{ (curve 2)}$  in (a) linear and (b) double logarithmic scales [86].

the coating by reducing the concentration of hydroxide ions adsorbed on the oxide surface. With an increase in the sodium silicate concentration, the electrolyte resistance increases; therefore, the breakdown voltage of the coating increases, as well as the microdischarge intensity [86]. The relationship between breakdown voltage and electrolyte conductivity during MAO is described by the empirical regression formula proposed in [91]. For other electrolytes, similarly, there are components that contribute to the coating dissolution and suppress this process. For example, in the case of an aluminate electrolyte, an increase in the electrolyte conductivity occurs with an increase in the sodium aluminate concentration [85]. In a borate-phosphate electrolyte, the coating dissolution at high temperatures is facilitated by borate ions, while phosphate ions promote uniform growth of the coating [122]. In some electrolytes, a decrease in conductivity and an increase in the breakdown voltage of the coating are observed when nanoparticles are added [91].

When describing the effect of the electrolyte composition on the MAO coating properties, instead of the components' concentration, the hydrogen exponent pH is sometimes used. However, the physical meaning of the regularities under consideration does not change in this case, since the pH of the electrolyte is related to the ions' concentration. For example, an increase in the concentration of nanoparticles leads to an increase in pH and a decrease in electrolyte conductivity [91]; as the pH of the electrolyte increases, the growth rate increases and the coating thickness increases [141], which agrees with the model described above. Typically, the pH of the electrolyte for MAO is 12.0–12.8, which indicates the alkaline nature of the solution [141].

Let us consider the influence of the electrolyte composition on the thickness, porosity, and surface roughness

using the example of MAO coatings formed on a magnesium alloy in an electrolyte containing titanium oxide nanoparticles. Thus, with an increase in the concentration of nanoparticles in the electrolyte, thickness, porosity, pore size, and surface roughness increase (Figures 23 and 24). In this particular case, the wettability of the coating surface is also increased, since titanium oxide has pronounced hydrophilic properties [142]. Corrosion resistance decreases in this case, which is associated with an increase in porosity, surface wettability and the presence of internal coating defects, as well as with a high mass fraction of amorphous oxides [91].

The influence of the electrolyte components concentration on the wear resistance of coatings is also ambiguous. Thus, at low concentrations of nanoparticles in the electrolyte, an increase in microhardness is observed; therefore,

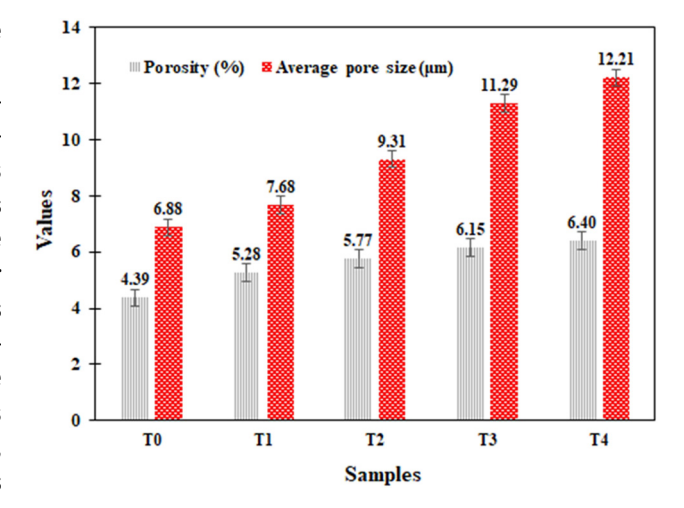


**Figure 23:** The average percentage of porosity and the average size of porosity with increasing concentration of  $TiO_2$  nanoparticles [91]:  $T_0 = 0$  g·L<sup>-1</sup>,  $T_1 = 1$  g·L<sup>-1</sup>,  $T_2 = 2$  g·L<sup>-1</sup>,  $T_3 = 3$  g·L<sup>-1</sup>, and  $T_4 = 4$  g·L<sup>-1</sup>.

20 — Ekaterina Pecherskaya *et al.* DE GRUYTER

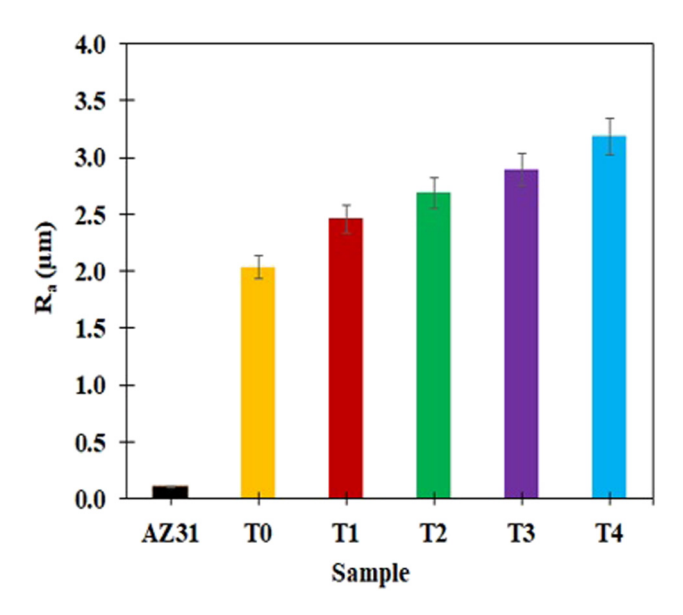


**Figure 24:** The surface roughness values of PEO-coated specimens at various concentrations of TiO<sub>2</sub>:  $T_0 = 0$  g·L<sup>-1</sup>,  $T_1 = 1$  g·L<sup>-1</sup>,  $T_2 = 2$  g·L<sup>-1</sup>,  $T_3 = 3$  g·L<sup>-1</sup>, and  $T_4 = 4$  g·L<sup>-1</sup> [91].

wear resistance increases; however, when a certain threshold value is exceeded, wear resistance decreases due to an increase in coating porosity [91]. A similar dependence is also characteristic of the adhesion strength of coatings: the adhesion strength increases with the concentration of electrolyte components; however, there is a critical concentration, above which the adhesion strength of coatings remains at a constant level [141].

The choice of electrolyte for MAO largely depends on the technologist experience, and is determined by the application area of the coatings, as well as the material of the initial alloy [119]. Let us explain it with an example. MAO coatings obtained in three electrolytes: phosphate, aluminate, and silicate have comparable anticorrosion and photocatalytic properties. At the same time, the most promising for MAO processing of the Ti<sub>6</sub>Al<sub>4</sub>V titanium alloy is a phosphate electrolyte, which provides a high formation efficiency (the ratio of the specific power supplied to the sample to the coating thickness) and a low breakdown voltage of the coatings. In addition, coatings obtained in a phosphate electrolyte contain only crystalline modifications of titanium oxide, while treatment in aluminate and silicate electrolytes leads to an increase in the content of amorphous phases in the coating [111].

### 4.6 Influence of electrolyte temperature

Let us consider the mechanism of influence of the silicatealkaline electrolyte temperature on the formation of oxide layers during MAO. The electrolyte temperature affects the breakdown voltage of the coating (there is a direct correlation), which is associated with a change in the ionic conductivity of the electrolyte [143]. As the electrolyte temperature decreases, the average size, brightness, and power of microdischarges decrease (Figure 25), that contributes to the

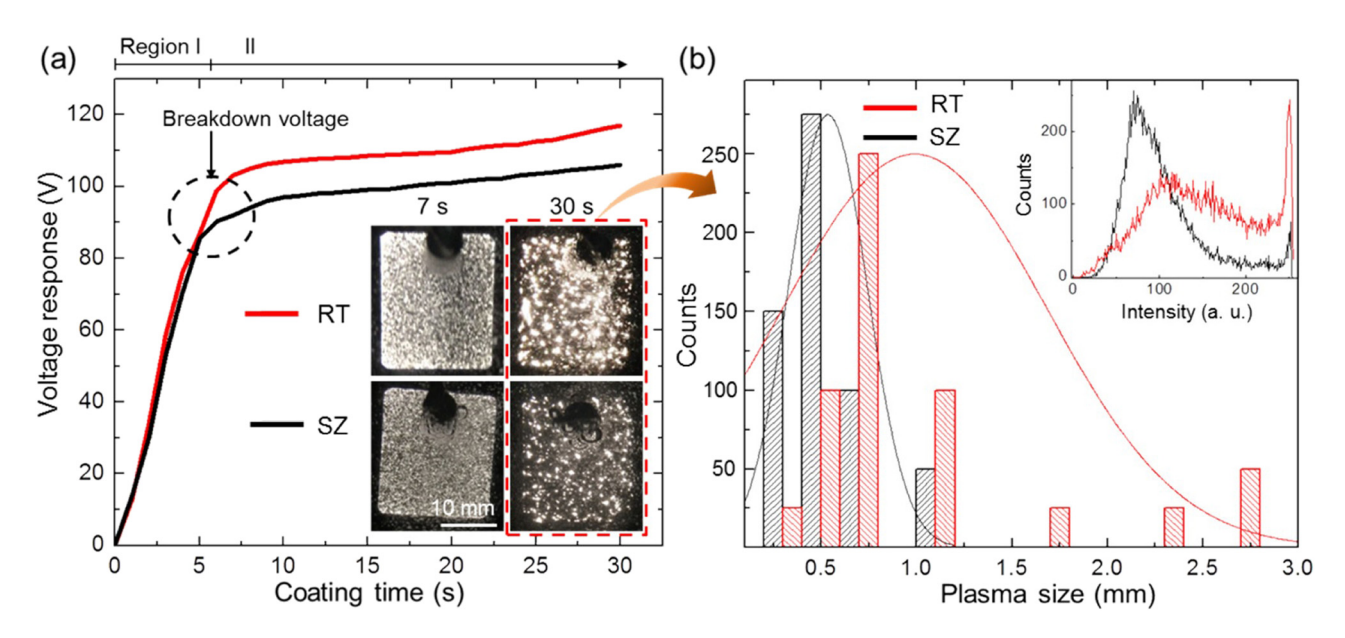


**Figure 25:** (a) Voltage–time curves of pure magnesium during MAO in electrolyte temperatures of 25°C and –5°C. The insets show the micro-discharges appearances at different coating times, at the onset of dielectric breakdown and at the final stage of MAO. (b) The histogram of size distribution and fraction of plasma discharges with inset describes their fraction of plasma intensities [124].

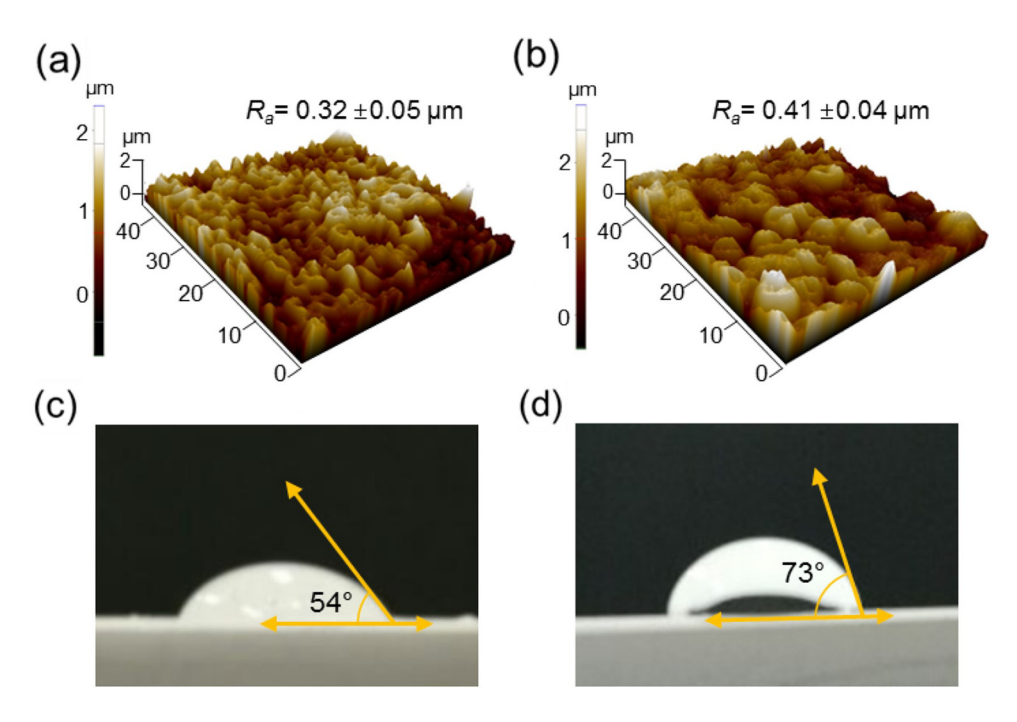


Figure 26: AFM images showing the surface roughness of the oxide layer formed on pure magnesium via MAO in two different electrolyte temperatures of (a)  $-5^{\circ}$ C and (b) 25°C. Water contact angles of oxide layers in sample, obtained at: (c)  $-5^{\circ}$ C and (d) 25°C [124].

transition to the "soft sparking" mode by reducing the size of the thermally activated zone around the microdischarge channel and increasing the rate of oxide crystallization.

The electrolyte temperature also affects the pore configuration and surface porosity. With an increase in temperature, the probability of the microdischarge cascade appearance increases, under the action of which large accumulations of united micropores are formed. As a result, the coating obtained at a higher electrolyte temperature has increased porosity, surface roughness, and has hydrophobic properties (Figure 26).

The dependence of the corrosion resistance of coatings on the electrolyte temperature for the MAO process differs from that for traditional anodizing [144]. It is known that for anodizing, the formation of coatings at low temperatures leads to a significant increase in their corrosion resistance. It was found, however, that no such effect is observed in the case of MAO, and the corrosion resistance of coatings obtained at low and high electrolyte temperatures is comparable [124].

### 4.7 Interaction of influencing factors

It is known that heterogeneous factors of the MAO process have a cumulative effect on the properties of MAO coatings. As a result, some factors are interdependent. An obvious example of this behavior is the relationship between current density and treatment time: with increasing current density, the treatment time is significantly reduced (Figure 27) [123].

Coating properties can also have mutual influence on each other. In particular, the coating thickness is in direct correlation with microhardness and adhesive strength [85]. With an increase in thickness, porosity and surface roughness of the coatings also increase, and the corrosion resistance decreases due to damage to the barrier layer by microarc discharges. With an increase in porosity and

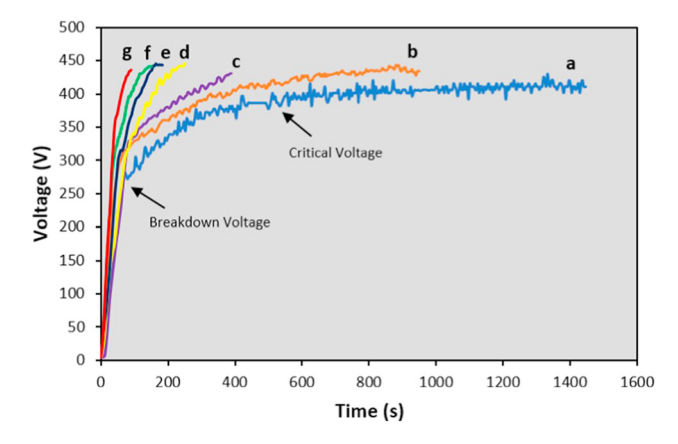


**Figure 27:** Voltage vs time plots obtained during PEO of titanium at current densities of (a) 30, (b) 40, (c) 50, (d) 60, (e) 80, (f) 100, and (g)  $120 \text{ mA} \cdot \text{cm}^{-2}$  [123].

pore diameter in coatings, an increase in the friction coefficient is observed [71].

#### 4.8 Influence of oxidation modes

There are three main modes of MAO coating deposition: galvanostatic, potentiostatic, and pulsed [1]. The potentiostatic mode assumes that the formation of coatings is carried out at a constant amplitude voltage applied to the galvanic cell. In this case, microdischarges burn over the entire surface of the sample, and their intensity increases with time. In the potentiostatic mode, as the coating grows, the current through the sample gradually decreases; it reduces the voltage drop across the coating. If the voltage drop becomes lower than the breakdown voltage of the oxide layer, the coating formation stops and the microdischarges are extinguished. In some cases (at a voltage of 400 V and a current density of 2 kA·m<sup>-2</sup>), microdischarges may not be observed on the sample surface, but burn inside the coating pores (Figure 28).

In the potentiostatic mode, with increasing voltage, the thickness and roughness of the coating surface increase, while the pore diameter and friction coefficient decrease [110].

In the galvanostatic mode (with direct current through the galvanic cell), a decrease in the forming voltage is also observed with a long processing time, accompanied by the microdischarge extinction (Figure 29). These phenomena precede the transition of the MAO process to the stage of arc discharges. In contrast to the potentiostatic mode, in the galvanostatic one, microdischarges are distributed unevenly over the sample surface, and their area increases with time [145].

In the galvanostatic mode, with increasing current density, thickness and porosity of the coatings increase, and the resistivity decreases (obviously, due to an increase in porosity). The surface roughness and the coefficient of coatings friction also decrease, which is apparently related to the coating compaction [1].

The pulse mode is devoid of the disadvantages of the two previous modes. In this mode, the microdischarges do not fade, since the energy is applied to the sample in short pulses. In this case, the average pulsed current turns out to be higher, other things being equal, leading to an increase in the current density by a factor of 4.5 [90]. Such a technological impact leads to an increase in the crystalline oxide content, thickness, wear resistance, and corrosion resistance of coatings [116,146].

The available data on the effect of heterogeneous factors on the MAO coating properties are summarized in Table 3.

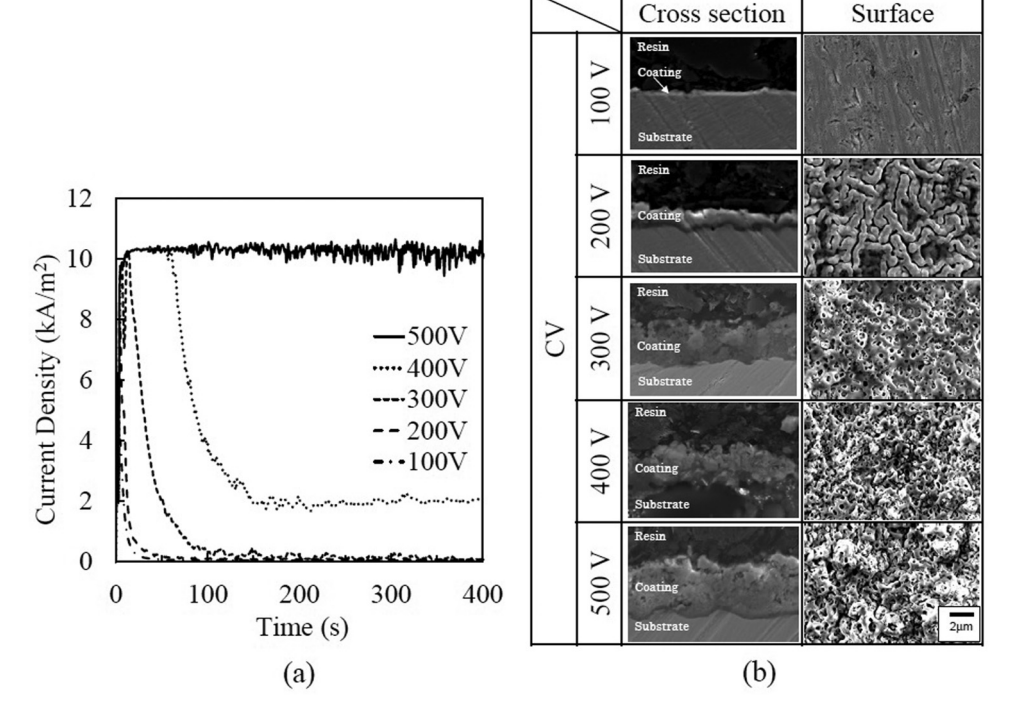


**Figure 28:** Current density and PEO coating of a Ti–15V–3Cr–3Sn–3Al titanium alloy by constant voltage (CV) operation. (a) Time variation of current densities for a 400 s treatment time. (b) Cross-section and surface morphology of the PEO coating at a 60 s treatment time [90].

Table 3 shows that the vast majority of coating parameters are influenced by a group of factors: current density, pulse frequency and duty cycle, treatment time, component concentration, and electrolyte temperature. For all cases, the nature of the factors influence on the coating properties is known: direct correlation means that with an increase in the influencing factor, the coating parameter increases; inverse correlation means that as the influencing factor increases, the coverage parameter decreases. Most of the relationships presented in the table are quite logical and correspond to modern ideas about the mechanism of MAO coating formation. However, there are also controversial points. First, there is a discrepancy between the correlation type for the same dependencies obtained by different authors. For example, the dependence of surface roughness on current density (rows 6 and 32 of Table 3) is characterized simultaneously as a direct and inverse correlation. (The same flaw can be traced in lines 17 and 52). Second, the designations "direct" and "reverse correlation" adopted in the table are rather conditional and reflect only the fact that the functional dependence is increasing or decreasing, without indicating a specific type of mathematical function. For some dependences, however, the type of functional dependence is known, but there are discrepancies in the simulation results. Thus, in the study by Jangde et al. [88], the dependence of the coating thickness on the treatment time is described by a linear function, and in the study by Wang and Zhang [122], by a linear and exponential function, depending on the stage (lines 25 and 51). Third, the works listed in the table are unique, each of them has its own peculiarities in terms of the initial alloy, electrolyte composition, and used technological parameters of MAO processing. In particular, when considering the

influence of the electrolyte components concentration, it should be taken into account that different electrolyte compositions are used (lines 4, 16, 39, *etc.*). To eliminate these shortcomings, it is necessary to supplement and refine information on the effect of heterogeneous factors on the properties of MAO coatings, and to obtain this information, it is necessary to conduct a number of interconnected experiments to develop the technological process in laboratory conditions.

### 5 Mathematical description of the MAO process

In general, there are not many works devoted to the mathematical description of the MAO process. The available developments in this direction affect only certain classes of phenomena occurring during the formation of coatings, which is obviously associated with complexity and interdisciplinary nature of the study object. For example, in the research by Yerokhin *et al.* [141], the main focus is on studying the kinetics of electrode processes during the MAO of a titanium alloy and describing the chemical reactions that occur during the coating formation. In the study by Shi and Li [31], on the contrary, the main attention is paid to the thermodynamic description of the MAO process using the theory of a plasma discharge in a liquid at low temperature.

Various physical principles, laws, and analytical expressions are used to model the MAO coating formation. Thus, to

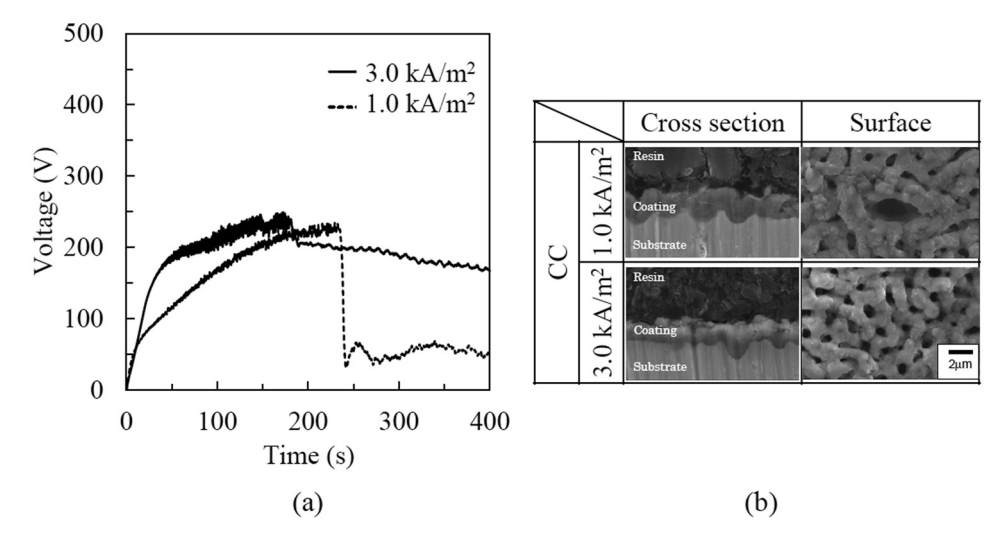


**Figure 29:** Voltage and PEO coating of a Ti–15V–3Cr–3Sn–3Al titanium alloy by constant current (CC) operation. (a) Time variation of the voltages for a 400 s treatment time. (b) Cross-section and surface morphology of a PEO coating at a 60 s treatment time [90].

Table 3: Influence of heterogeneous factors on the MAO coating properties

Š	Substrate material	Coating parameter	Influencing factor	Nature of influence	Ref.
_	A11050	Breakdown voltage	Apode current density	Does not affect	[86]
۰ ،	A10E0	Growth rate	Curront doneity	Growth rate increase linearly with current dencity	[2]
7 (	OCOLA	פוסאמון מנפ	Cullellt delisity	di Owii i late ilici eases illiearij with tuli ent delisity	<u> </u>
m	Al1050	Growth rate	Pulse trequency	No effect	[9]
4	Al1050	Breakdown voltage	Concentration of electrolyte	Strong inverse correlation	[86]
			components (NaOH)		
2	Al1050	Porosity	Treatment time	Inverse correlation (as the influencing factor increases, the	[49]
				coating parameter decreases)	
9	Al1050	Surface roughness	Current density	Direct correlation (as the influencing factor increases, the	[9]
				coating parameter increases)	
7	AI1050	Surface roughness	Pulse frequency	Inverse correlation	[9]
∞	Al1050	Surface roughness	Treatment time	Direct correlation	[49]
6	AMg2, D16T	Microhardness, plasticity	Composition of the original alloy	MAO coatings on aluminum alloys have a higher	[19]
				microhardness	
10	AI2214	Growth rate	Current density	Growth rate increases linearly with current density	[9]
Ħ	AI2214	Growth rate	Pulse frequency	No effect	[9]
12	AI2214	Surface roughness	Current density	Direct correlation	[9]
13	AI2214	Surface roughness	Pulse frequency	Inverse correlation	[9]
4	CP Ti	Porosity	Current density	Inverse correlation	[123]
15	CP Ti	Porosity	Pulse frequency	As the pulse frequency increases, the porosity of coatings	[123]
				decreases exponentially	
16	CP-Ti grade 2	Breakdown voltage	Concentration of electrolyte	Inverse correlation	[82]
			components (sodium aluminate)		
1	CP-Ti grade 2	Pore diameter	Processing time	No effect (at a given breakdown voltage)	[82]
8	CP-Ti grade 2	Pore density	Treatment time	Inverse correlation	[88]
19	CP-Ti grade 2	Microhardness	Coating thickness	Direct correlation	[85]
70	CP-Ti grade 2	Adhesion strength	Coating thickness	Direct correlation	[85]
71	VT1-0	Microhardness, plasticity	Composition of the original alloy	MAO coatings on titanium alloys are characterized by	[19]
				increased plasticity	
22	Ti- $xAI$ ( $x = 0, 3, 6, 10, 20$ wt%) alloys	Breakdown voltage	Composition of the initial alloy	With an increase in the aluminum content in the titanium	[105]
			(aluminum content in the titanium	alloy, the breakdown voltage increases linearly	
			alloy)		
23	Titanium fibers (5.5% Al, 3.5% V, 0.3%	Wear resistance, corrosion resistance	Sample shape	On fiber-shaped samples, the wear resistance and corrosion	[127]
	Fe, and balance Ti)			resistance of the coating are reduced due to cracking	
24	Ti-6Al-4V	Growth rate	Concentration of electrolyte	Direct correlation	[141]
			components		
25	Ti-6Al-4V	Thickness	Treatment time	At the stage of spark discharges, the dependence of the	[122]
				MAU coating unickness on the treatment time is described	
				by an exponential function, at the stage of microarc وانجاب المرابعة المرا	
				מוזיבות שלכי זר זי וווירמו	(Continued)

Table 3: Continued

Š.	Substrate material	Coating parameter	Influencing factor	Nature of influence	Ref.
36	Ti 6Al AV	17:17		Direct correlation	[1/1]
27	Ti-6AI-4V	Adhesion strength	Electrolyte Pri	The dependence increases to a threshold value then does	[141]
i			components	not change	7
28	Ti-6Al-4V	Surface roughness	pH of electrolyte	Inverse correlation	[141]
29	Ti-15V-3Cr-3Sn-3Al	Resistivity	Current density	Inverse correlation (in galvanostatic mode)	[06]
30	Ti-15V-3Cr-3Sn-3Al	Thickness	Current density	Direct correlation (in galvanostatic mode)	[66]
31	Ti-15V-3Cr-3Sn-3Al	Surface roughness	Forming voltage	Direct correlation (in potentiostatic mode)	[66]
32	Ti-15V-3Cr-3Sn-3Al	Surface roughness	Current density	Inverse correlation (in galvanostatic mode)	[06]
33	Ti-15V-3Cr-3Sn-3Al	Friction coefficient	Current density, forming voltage	Inverse correlation (in potentiostatic mode)	[06]
34	Mg (99.96%)	Breakdown voltage, porosity, surface	Electrolyte temperature	Direct correlation	[124]
		roughness			
35	Mg (99.96%)	Corrosion resistance	Electrolyte temperature	No effect	[124]
36	AZ63	Percentage of crystalline oxides,	Treatment time	Direct correlation	[49], [86]
		microhardness, corrosion resistance,			
		surface roughness			
37	AZ63	Porosity	Treatment time	Inverse correlation	[98]
38	AZ63	Microhardness, corrosion resistance	Porosity	Inverse correlation	[49]
39	AZ31	Thickness, porosity, pore diameter, surface	Concentration of electrolyte	Direct correlation	[91]
		roughness, and wettability	components (TiO <sub>2</sub> nanoparticles)		
40	AZ31	Corrosion resistance	Concentration of electrolyte	Inverse correlation	[91]
			components (TiO <sub>2</sub> nanoparticles)		
4	AZ31	Wear resistance	Concentration of electrolyte	The dependence is maximum	[91]
			components (TiO <sub>2</sub> nanoparticles)		
42	AZ31	Pore area, surface roughness	Coating thickness	Direct correlation	[71]
43	AZ31	Number of pores, corrosion resistance	Coating thickness	Inverse correlation	[71]
44	AZ31	Friction coefficient	Porosity	Direct correlation	[71]
45	AZ31	Friction coefficient	Pore diameter	Direct correlation	[71]
46	AZ31B	Percentage of crystalline oxides, thickness,	Pulse duty cycle	Direct correlation	[116]
		corrosion resistance			
47	AZ31B	Breakdown voltage, porosity	Duty cycle	Inverse correlation	[116]
48	E-Form	Pore area, surface roughness	Coating thickness	Direct correlation	[71]
49	E-Form	Number of pores, corrosion resistance	Coating thickness	Inverse correlation	[71]
20	E-Form	Friction coefficient	Porosity, pore diameter	Direct correlation	[71]
21	AM50	Thickness	Treatment time	Coating thickness increases linearly with processing time	[88]
52	AM50	Pore diameter	Treatment time	Direct correlation	[88]
23	AM50	Pore density	Treatment time	Inverse correlation	[82]
54	AM50	Pore area, surface roughness	Coating thickness	Direct correlation	[71]

Table 3: Continued

No.	No. Substrate material	Coating parameter	Influencing factor	Nature of influence	ا
55	55 AM50	Corrosion resistance, number of pores	Coating thickness	Inverse correlation [71]	1
99	56 AM50	Friction coefficient	Porosity, pore diameter	Direct correlation [71]	_
Alloy Fe, 0	/ compositions from Table 3: Al1050: 99.5 3.15 wt% Cu, 0.1–0.5 wt% Mn, 1.7–2.4 wt <sup>9</sup>	wt% Al, 0.25 wt% Si, 0.4 wt% Fe, 0.05 wt% Cu, % Mg, 0.05 wt% Cr, 0.15 wt% Zn, 0.15 wt% Ti	0.05 wt% Mn, 0.05 wt% Mg, 0.07 wt% Zr 0.15 wt% others, and balance Al (Al-N	Alloy compositions from Table 3: Al1050: 99.5 wt% Al, 0.25 wt% Si, 0.4 wt% Fe, 0.05 wt% Cu, 0.05 wt% Mn, 0.05 wt% Mg, 0.07 wt% Zn, 0.05 wt% Ti, 0.05 wt% Ti, 0.05 wt% Mg, 0.05 wt% Ti, 0.05 wt% Mg, 0.05 wt% Mn, 1.7-2.4 wt% Mg, 0.05 wt% Cr, 0.15 wt% Zn, 0.15 wt% Ti, 0.15 wt% Ti, 0.15 wt% Others, and balance Al (Al-Mg alloy). D16T: 0.5 wt% Si, 0.5 wt% Fe, 3.8-4.9 wt% Cu, 0.3-0.9 wt% Mn,	0.5 wt% t% Mn,

Fe, 0.003 wt% Ni, 0.3 wt% 97 wt% Mg, 6, 10, 20 wt%) alloys: 0, 3, 6, 10, 20 wt% Al and balance Ti Titanium fibers: 5.5% Al, 3.5% Al, 3.5% V, 0.3% Fe, and balance Ti (Ti–Al–V alloy). Ti–15V–3Cr–3Sh–3Al: Fe, 3.9-5 wt% Cu, 0.4-1 wt% Mn. 2.5-3.5 wt% AI, 0.6-1.4 wt% Zn, 0.2 wt% Mn, 0.1 wt% Si, 0.05 wt% Cu, 0.04 wt% Ca, 0.005 wt% Fe, 0.005 wt% Ni (extruded Mg-Al alloy). E-Form is AZ31 magnesium alloy with additional Ca. AM50: 94.8 wt% Mg 0.25 wt% 0, 0.015 wt% H, 0.03 wt% N (commercially pure titanium). VT1-0: 99.58 wt% Ti, 0.15 wt% Fe, 0.05 wt% C, 0.08 wt% Si, 0.04 wt% N, 0.1 wt% O, 0.008 wt% H (commercially pure titanium). TI-xAl (x = 0, 0.2-0.8 wt% Mg, 0.1 wt% Cr, 0.25 wt% Zn, 0.15 wt% Ti, 0.05 wt% Zr, 0.15 wt% others (Al-Cu-Si aluminum wrought alloy). CP-Ti: commercially pure titanium. CP-Ti grade 2: 92.2 wt% Ti, 0.1 wt% C, 0.3 wt% Ii, 0.1 wt% C, 0.3 wt% Ii) Fe, and balance Mg (extruded Mg-Al alloy). AZ31B: Mg (99.96%): pure magnesium. AZ63: 5–7 wt% AI, 2–4 wt% Zn, 0.15 wt% Mn, 0.1 wt% Cu, 0.3 wt% Si, 0.003 wt% 1.2-1.8 wt% Mg, 0.1 wt% Cr, 0.25 wt% Zn, 0.15 wt% Ti, 0.05 wt% Zr, 0.15 wt% others, and balance Al (Al-Cu-Mg alloy). Al2214: 90.8-95 wt% Al, 0.5-1.2 wt% Si, 0.7 w Si, 0.003 wt% Cu, 0.0012 wt% Ni, 0.0023 wt% Zn, 0.4 wt% Mn, 0.02 wt% 4.4–5.4 wt% Al, 0.26–0.6 wt% Mn, 0.22 wt% Zn, 0.1 wt% Si (Al–Mn cast magnesium alloy) others, and balance Mg (Mg–Al alloy). AZ31: 3.05 wt% Al, 0.82 wt% 15 at% V, 3 at% Cr, 3 at%

study microplasma processes, the model of local thermodynamic equilibrium, the Saha and Boltzmann equations, and the Maxwell energy distribution are used [83]. The theory of inelastic collisions of gas molecules is used to describe the mechanism of the microdischarge appearance [31]. The excess pressure of electrolyte vapors in the bubble during microdischarge combustion is calculated using the Rayleigh-Plesset equation [22]. The ionic conductivity of an electrolyte is determined using the Arrhenius theory of conductivity [124]. To describe the valve effect at the stage of formation of the barrier coating layer, the band diagrams of the "metal-oxide-electrolyte" system are used (Figure 30) [147]. Using the Joule-Lenz law, relations that relate the volume of a gas-vapor bubble to the electrolyte temperature and power dissipation were obtained [124]. Expressions for calculating the growth rate, grain size, and MAO coating thickness by the iterative method using Fick's second diffusion law were proposed [131]. Calculation formulas to determine the amount of heat required for melting, evaporation, and heating of the oxide layer at the bottom of the pore to the plasma temperature were obtained [124].

For the MAO process, as well as for anodization, Faraday's law for electrolysis is fulfilled. In this case, when calculating the coating thickness, one should take into account the total charge density that passed through the anode during processing (Figure 31). Two sections can be distinguished in the figure: steep and gentle. The steep section, where a sharp increase in the total charge density occurs, corresponds to the formation of a barrier and porous oxide layer and can be approximated by an exponential function. The gentle section, which appears at voltages less than 400 V, corresponds to saturation (the charge density is almost constant, the coating thickness does not change), and is approximated by a linear function. In this case, the total charge density increases with increasing voltage and current density, and the maximum charge density can increase the input current density by three times.

It should be noted that when calculating the coating thickness according to the Faraday law, the phenomena of the formation of gas-vapor bubbles on the anode (which consume 85% of the input current density) and the microdischarge combustion inside the pores are not taken into account. In this regard, when calculating, it is necessary to take into account the efficiency factor for using the total charge density, which does not exceed 15%. This coefficient decreases with an increase in the voltage between the anode and cathode, which is associated with increased gas release and the formation of an internal porous structure [90].

**Table 4:** Technological parameter values of the MAO process of titanium for forming curves are shown in Figure 35 [121]

Sample	Current density (A·m <sup>-2</sup> )	Ton	T <sub>off</sub>	Duty cycle (%)
30T5/10	3,000	50	100	67
38T5/10	3,800	50	100	67
45T5/10	4,500	50	100	67
30T10/5	3,000	100	50	33
38T10/5	3,800	100	50	33
45T10/5	4,500	100	50	33

### 5.1 Modeling the forming curve

An important area of the MAO process research is the forming curve modeling which makes it possible to analytically describe changes in the mechanism of oxide coating formation with time. It has been shown, *e.g.*, that at the stages of anodization and microarc discharges, the forming curve is approximated by linear functions, and at the stage of spark discharges – by exponential functions (Figure 32) [122]. In this

case, the slope of the forming curves reflects the coating resistance at different stages of its formation. No micro-discharges are observed at the anodizing stage, the coating thickness increases due to the ion current according to the Faraday law for electrolysis; coating resistance increases rapidly. At the stage of spark discharges, the coating growth rate and the slope of the forming curves decrease, since part of the current is spent to maintain the microdischarge combustion; the coating resistance increases much more slowly. At the stage of microarc discharges, the coating is already formed, its resistance does not change; at this stage, only high-temperature phase transitions of amorphous to crystal-line oxides occur due to local heating of the inner regions of the coating at the sites of microdischarges [123].

The results of the forming curves study make it possible to formulate the following theoretical statements describing the mechanism of coating formation:

- (1) the growth of the coating thickness occurs only due to the ion current;
- (2) the microdischarge resistance is negligible;

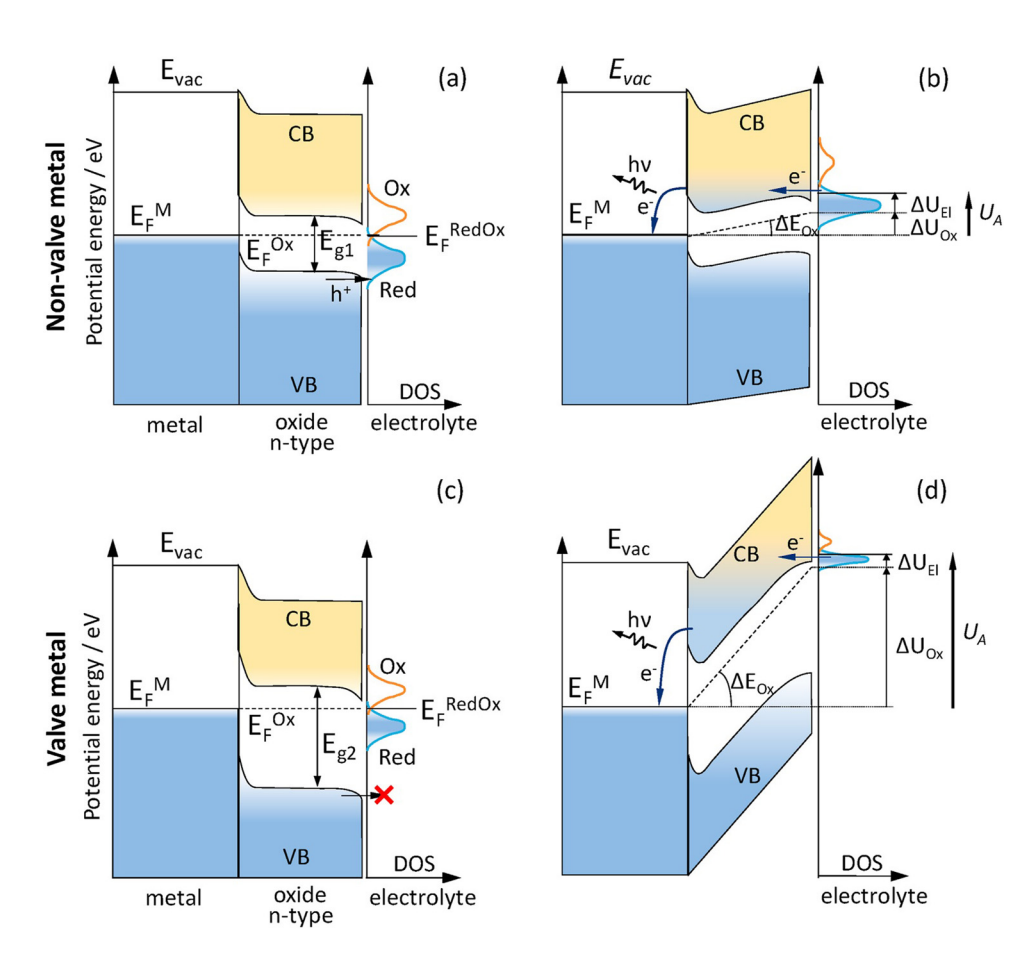


**Figure 30:** Examples of simplified band diagrams for metal-oxide electrode formed on (a) and (b) non-valve and (c) and (d) valve metals under (a) and (c) open cell and (b) and (d) anodic polarization ( $U_A$ ). Not to scale.  $E_{\text{vac}}$  – vacuum level of electron energy.  $E_F^M$ ,  $E_F^{OX}$ , and  $E_F^{\text{RedOX}}$  – electrons Fermi level in metal, oxide, and solvated redox species. Band gaps relation:  $E_{\text{q1}} < E_{\text{q2}}$ .  $\Delta E_{\text{OX}}$  – electric field across oxide. DOS – density of states [147].

28 — Ekaterina Pecherskaya *et al.* DE GRUYTER

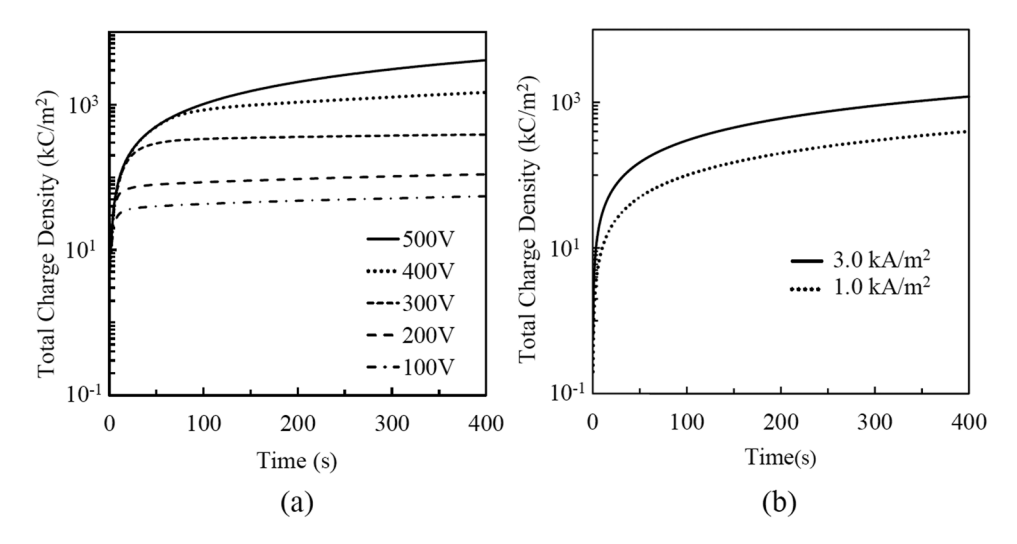


Figure 31: Time variation of the total charge density during the PEO process by (a) CV operation and (b) CC operation [90].

(3) the microdischarge ignition occurs by avalanche breakdown of the formed coating.

These provisions make it possible to independently consider the electrochemical and microplasma processes and are useful in the development of mathematical models of the MAO process [123].

### 5.2 Influence of heterogeneous factors on the shape of the forming curve

The forming curve is important not only for the analytical description of the MAO process, but also for predicting the properties of the resulting coatings [135]. First, the forming voltage is a derivative of the current and the coating resistance and, in fact, does not belong to the influencing factors of the MAO process. Second, the forming curve is an integral characteristic that contains complete information about all the phenomena that accompany the coating formation, including the influence of heterogeneous factors on the coating properties. Third, the forming curve is measured in real time, which makes it possible to predict the course of the MAO process and obtain primary information about the coating properties already at the stage of their formation. Let us consider possible practical applications of the forming curve for the MAO process analysis.

(1) Determination of the possibility of conducting the MAO process. It is known that the formation of high-quality MAO coatings occurs only at a certain combination of technological parameters. For example, during the MAO of aluminum in the galvanostatic mode, microdischarges can occur only when coatings are deposited in weakly

alkaline electrolytes at high voltage [86]. Practical experience shows that high-quality MAO coatings are obtained if the forming curve has a classical form, as shown in Figure 33. (This particular case corresponds to a coating with a microhardness of 11.5 GPa, which has high wear resistance) [146]. With incorrectly selected technological parameters, the forming curve has a distorted form, as, *e.g.*, in Figure 34. The graph shows a deep local minimum at the microdischarge stage, after which the voltage does not recover to its previous values, but remains at a level of about 220 V. During a local minimum, sparking stops, and when the voltage is restored, the intensity and

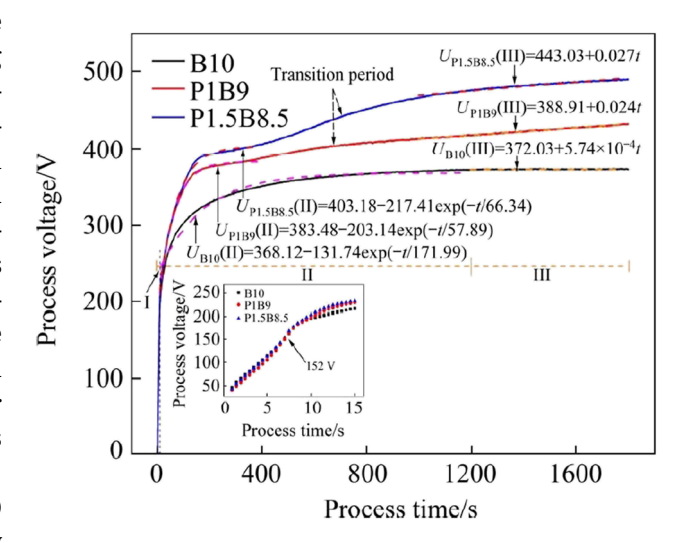


**Figure 32:** Process voltage of  $Ti_6Al_4V$  alloy treated by MAO in P/B electrolyte [122]. Electrolyte composition: for sample B10:  $Na_2B_4O_7$  (0.1 mol· $L^{-1}$ ); for sample P1B9:  $Na_2B_4O_7$  (0.09 mol· $L^{-1}$ ) and  $Na_3PO_4$  (0.01 mol· $L^{-1}$ ); and for sample P1.5B8.5:  $Na_2B_4O_7$  (0.015 mol· $L^{-1}$ ) and  $Na_3PO_4$  (0.085 mol· $L^{-1}$ ).

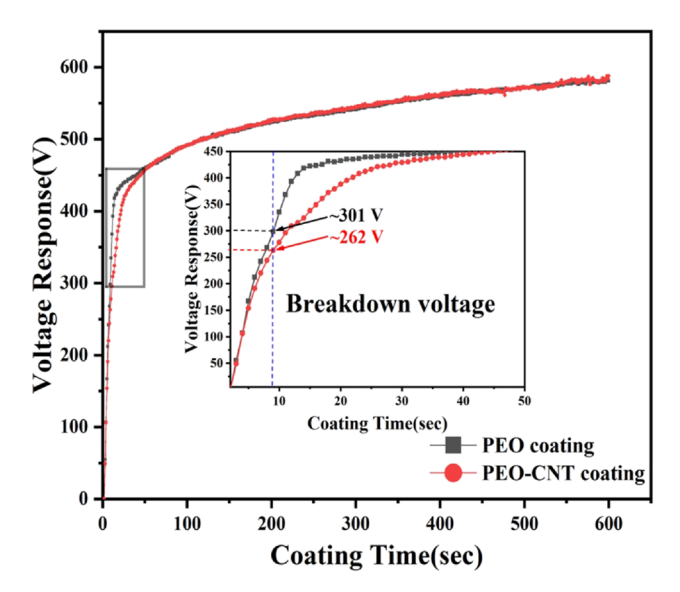


**Figure 33:** Time–voltage responses for PEO process of AZ91 Mg alloy [146].

number of microdischarges are significantly reduced; there is also a constant evolution of gas. In this case, a loose coating of white color is formed on the entire surface of the sample. The resulting coating consists of two layers: a thin porous inner layer of titanium oxide and a thick porous outer layer of amorphous silicon oxide, and has low wear resistance [148]. Thus, the appearance of the forming curve can serve as an indicator of the MAO coating quality.

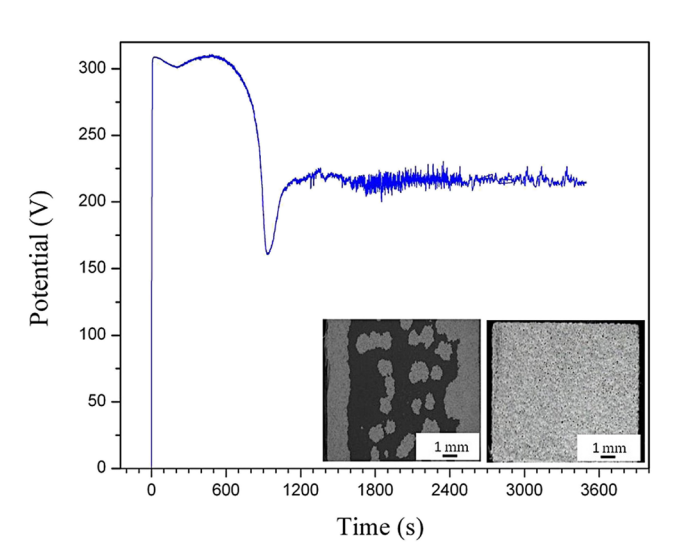


**Figure 34:** Cell voltage during PEO of titanium for 3,600 s at 500 mA·cm<sup>-2</sup>, with a frequency of 50 Hz, a duty cycle of 50%, and a negative-to-positive current ratio of 1. Inset: photographs of specimens after PEO for 180 and 700 s [148].

(2) Prediction of the formed coating properties. The influence of heterogeneous factors, which leads to a change in the properties of coatings, is displayed on the forming curve. Thus, *e.g.*, the current density and electrolyte composition have different effects on the course of the forming curve.

The effect of current density and duty cycle on the shape of the forming curve can be described as follows. An increase in the current density and a decrease in the duty cycle of the pulses lead to an increase in the steepness of the forming curve at all stages of the MAO process, and in general, the forming voltage (Figure 35). In this case, the transition time to the next stage of the MAO process, which corresponds to the critical points of the forming curve (breakdown voltage, critical voltage, final voltage), decreases with current density [86,121].

In addition, the form of the forming curve is affected by the electrolyte conductivity, which is determined by the concentration of its components, and also depends on temperature. At the stage of spark discharges, with a decrease in electrolyte conductivity, the forming voltage, the steepness of the forming curve [88], and the breakdown voltage of the coating increase, and the duration of the stage decreases (Figure 36) [122]. At the stage of microarc discharges, an increase in the forming stress is also observed; the steepness of the forming curve at this stage is practically independent of the electrolyte conductivity [86,121]. At the anodization stage, the steepness of the forming curve and the

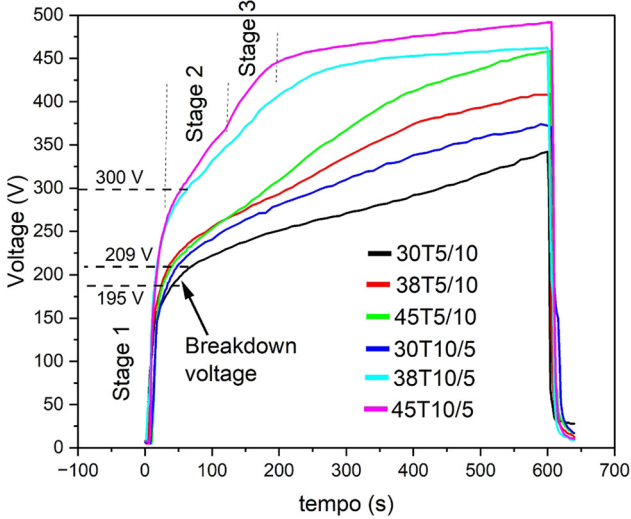


**Figure 35:** Forming curves of the MAO process for titanium at various parameters of the technological mode (current density, pulse duration and pause, pulse duty cycle). The samples names in the figure correspond to different sets of the technological parameter values for obtaining MAO coatings, given in Table 4 [121].

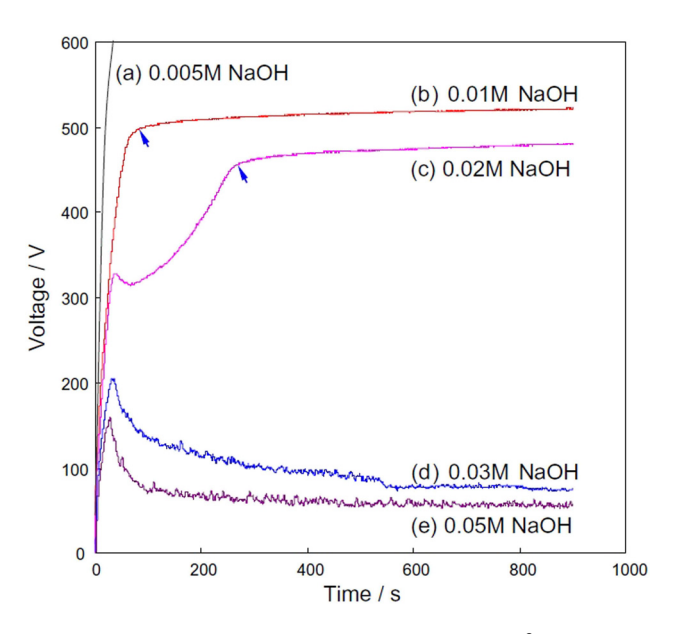


**Figure 36:** Voltage–time curves of aluminum at 10  $\text{A}\cdot\text{dm}^{-2}$  in (a) 0.0005 M, (b) 0.01 M, (c) 0.02 M, (d) 0.03 M, and (e) 0.05 M NaOH solutions [86].

breakdown voltage of the coating do not depend on the electrolyte (Figure 32) [122]. As the temperature rises, the electrolyte conductivity increases, while the breakdown voltage decreases [124].

Considering the foregoing and using the dependences of coating properties on influencing factors considered in Section 4, we can assume the following:

- (a) A change in the steepness of the forming curve indicates a change in the rate of increase in the coating thickness. At the same time, at the anodization stage, the growth rate of the coating thickness does not depend on the composition of the electrolyte and is determined by the electrical parameters of the MAO process (current density and pulse duty cycle) [122,146]. At the stage of microarc discharges, the slope of the forming curves depends weakly on the current density [86]. In some cases, a slight increase in the growth rate of the coating thickness is observed. At the stage of arc discharges, the growth rate of the coating thickness does not depend on the current density [83].
- (b) An increase in the forming voltage also indicates an increase in the coating thickness and leads to an increase in the microdischarge intensity. It increases the content of crystalline oxides, microhardness, wear resistance, and corrosion resistance of coatings, while porosity decreases.
- (c) A decrease in the duration of the spark discharge stage indicates a change in the ratio of the electron and ion currents. In this case, according to the steepness of the

forming curve at the stage of spark discharges, one can indirectly judge the proportion of the ion current, which provides an increase in the coating thickness. The electron current in this case can be expressed as the difference between the total current passing through the galvanic cell (measured during oxidation) and the ionic current calculated according to Faraday's law using the forming curve. Knowing the electron and ion currents and varying the electrical parameters of the process and the concentration of electrolyte components, it is possible to control the intensity of electrochemical and microplasma processes in order to obtain the required coating properties.

Thus, the forming curve contains information about the properties of MAO coatings and serves as an effective tool for their prediction. However, the proposed method for predicting the coating properties is not without drawbacks. It is obvious, for example, that the same change in the forming curve corresponds to a change in various factors under which the properties of the formed coatings can also differ. To eliminate this shortcoming, it is advisable to use neural network algorithms that perform an automated selection of technological parameters.

#### 6 Conclusion

Currently, the MAO technology is undergoing significant changes: the range of processed materials is expanding, new areas of oxide coating application are opening up, new processing modes and modified technological processes are emerging. However, some scientific and technical problems in this area still remain unresolved, which leads to a limitation in the practical application of the MAO process due to high energy consumption and low controllability. The main problem of a fundamental nature is the insufficient knowledge of the mechanism of microarc oxide coating formation, which is associated with the interdisciplinary nature of the study object. There are various interpretations of the coating formation mechanism which differ, first of all, in the description of the microdischarge occurrence and combustion process. An analysis of existing mathematical models has shown that at present there is no generalized analytical description of the MAO process. The available mathematical models reveal only certain aspects of the coating formation; however, they make it possible to identify prerequisites, recommendations, and theoretical provisions that can be used in the development of a complex mathematical model underlying the digital twin of the MAO process.

In addition, it is of great practical importance to study the regularities of the heterogeneous factors influence on the oxide layer properties in order to select the optimal technological parameters of the coating process. The analysis of these regularities made it possible to detect discrepancies in the results of studies by different authors, which are due to the technological features of the coating formation process, their area of application, as well as the specifics of the scientific problems being solved. In addition, it is shown that not all of the considered relationships have an analytical description. In this regard, it is necessary to supplement and refine the available data on the relationship between heterogeneous influencing factors and MAO coating parameters.

A convenient tool for studying and modeling the MAO process is the forming curve, the shape of which makes it possible to judge the mechanism of oxide layer growth under the influence of influencing factors and contains information about the properties of the formed coatings. It makes it possible to use the forming curve to determine the correct choice of technological parameters and predict the properties of oxide coatings in the process of their formation. When the existing shortcomings are eliminated using neural network algorithms, this method can be highly effective in selecting the optimal technological parameters for the process of applying microarc oxide coatings with desired properties.

**Funding information:** The work was supported by the grant from the Ministry of Science and Higher Education of the Russian Federation № 1022041100284-5-2.3.1. "Fundamentals of the digital twin of the technological process of forming oxide coatings with specified properties by microarc oxidation."

**Author contributions:** All authors have accepted responsibility for the entire content of this manuscript and approved its submission.

**Conflict of interest:** The authors state no conflict of interest.

**Data availability statement:** The datasets generated and/ or analyzed during the current study are available from the corresponding author on reasonable request.

### References

[1] Li, G., F. Ma, P. Liu, S. Qi, W. Li, K. Zhang, et al. Review of micro-arc oxidation of titanium alloys: Mechanism, properties and applications. *Journal of Alloys and Compounds*, Vol. 948, 2023, id. 169773.

- [2] Rodriguez, L., J. Y. Paris, J. Denape, and K. Delbé. Micro-arcs oxidation layer formation on aluminium and coatings tribological properties—A review. *Coatings*, Vol. 13, No. 2, 2023, id. 373.
- [3] Yao, W., L. Wu, J. Wang, B. Jiang, D. Zhang, M. Serdechnova, et al. Micro-arc oxidation of magnesium alloys: A review. *Journal of Materials Science & Technology*, Vol. 118, 2022, pp. 158–180.
- [4] Simchen, F., M. Sieber, A. Kopp, and T. Lampke. Introduction to plasma electrolytic oxidation—An overview of the process and applications. *Coatings*, Vol. 10, No. 7, 2020, id. 628.
- [5] Blawert, C., S. P. Sah, N. Scharnagl, and M. B. Kannan. Plasma electrolytic oxidation/micro-arc oxidation of magnesium and its alloys, Elsevier eBooks, Cambridge, UK, 2015, pp. 193–234.
- [6] Martin, J., A. Melhem, I. Shchedrina, T. Duchanoy, A. Nominé, G. Henrion, et al. Effects of electrical parameters on plasma electrolytic oxidation of aluminium. Surface and Coatings Technology, Vol. 221, 2013, pp. 70–76.
- [7] Shirani, A., T. Joy, A. B. Rogov, M. Lin, A. Yerokhin, J. E. Mogonye, et al. PEO-Chameleon as a potential protective coating on cast aluminum alloys for high-temperature applications. *Surface and Coatings Technology*, Vol. 397, 2020, pp. 126016–126016.
- [8] Yang, C., H. Cai, S. Cui, J. Huang, J. Zhu, Z. Wu, et al. A zinc-doped coating prepared on the magnesium alloy by plasma electrolytic oxidation for corrosion protection. *Surface and Coatings Technology*, Vol. 433, 2022, id. 128148.
- [9] Yao, R., Y. Li, Z. Yao, P. Zhang, S. Lu, and X. Wu. Black PEO coating with enhanced thermal stability on titanium alloy and its thermal control properties. *Surface and Coatings Technology*, Vol. 429, 2022, id. 127934.
- [10] Baranova, T. A., A. K. Chubenko, A. I. Mamaev, V. A. Mamaeva, and Y. B. Kovalskaya. Construction of layered structures on valve metal alloys by microplasma oxidation. *IOP Conference Series: Materials Science and Engineering*, Vol. 156, No. 1, 2016, id. 012013.
- [11] Shore, D., J. C. Avelar-Batista Wilson, A. Matthews, and A. Yerokhin. Adhesive bond strength of PEO coated AA6060-T6. Surface and Coatings Technology, Vol. 428, 2021, id. 127898.
- [12] Fattah-alhosseini, A., R. Chaharmahali, K. Babaei, M. Nouri, M. K. Keshavarz, and M. Kaseem. A review of effective strides in amelioration of the biocompatibility of PEO coatings on Mg alloys. *Journal of Magnesium and Alloys*, Vol. 10, No. 9, 2022, pp. 2354–2383.
- [13] Sowa, M., M. Parafiniuk, C. M. S. Mouzêlo, A. Kazek-Kęsik, I. S. Zhidkov, A. I. Kukharenko, et al. DC plasma electrolytic oxidation treatment of gum metal for dental implants. *Electrochimica Acta*, Vol. 302, 2019, pp. 10–20.
- [14] Fattah-alhosseini, A., M. Molaei, M. Nouri, and K. Babaei. Antibacterial activity of bioceramic coatings on Mg and its alloys created by plasma electrolytic oxidation (PEO): A review. *Journal of Magnesium and Alloys*, Vol. 10, No. 1, 2021, pp. 81–96.
- [15] Zolotarjovs, A., K. Smits, K. Laganovska, I. Bite, L. Grigorjeva, K. Auzins, et al. Thermostimulated luminescence of plasma electrolytic oxidation coatings on 6082 aluminium surface. *Radiation Measurements*, Vol. 124, 2019, pp. 29–34.
- [16] Wu, H. C., J. Jiang, and E. I. Meletis. Microstructure of BaCO<sub>3</sub> and BaTiO<sub>3</sub> coatings produced on titanium by plasma electrolytic oxidation. *Applied Surface Science*, Vol. 506, 2020, id. 144858.
- [17] Kaseem, M., T. Zehra, B. Dikici, A. Dafali, H. W. Yang, and Y. G. Ko. Improving the electrochemical stability of AZ31 Mg alloy in a 3.5wt.% NaCl solution via the surface functionalization of plasma electrolytic oxidation coating. *Journal of Magnesium and Alloys*, Vol. 10, No. 5, 2021, pp. 1311–1125.

- [18] Chubenko, A. K., T. A. Baranova, Y. N. Dolgova, V. A. Mamaeva, and A. I. Mamaev. Synthesis of non-metallic inorganic radiationabsorbing coatings on the surface of VT1-0 titanium alloy. IOP Conference Series: Materials Science and Engineering, Vol. 511, No. 1, 2019, id. 012035.
- [19] Arbuzova, S. S., P. I. Butyagin, A. V. Bol'shanin, A. I. Kondratenko, and A. V. Vorob'ev. Microarc oxidation of metal surfaces: Coating properties and applications. Russian Physics Journal, Vol. 62, No. 11, 2020, pp. 2086-2091.
- Saji, V. S.. Superhydrophobic surfaces and coatings by electro-[20] chemical anodic oxidation and plasma electrolytic oxidation. Advances in Colloid and Interface Science, Vol. 283, 2020, id. 102245.
- [21] Abdulkareem AlMashhadani, H., A. A. Khadom, and M. M. Khadhim. Effect of Polyeugenol coating on surface treatment of grade 23 titanium alloy by micro arc technique for dental application. Results in Chemistry, Vol. 4, 2022, id. 100555.
- [22] Troughton, S. C., A. Nominé, A. V. Nominé, G. Henrion, and T. W. Clyne. Synchronised electrical monitoring and high speed video of bubble growth associated with individual discharges during plasma electrolytic oxidation. Applied Surface Science, Vol. 359, 2015, pp. 405-411.
- [23] Dehnavi, V., B. L. Luan, D. W. Shoesmith, X. Y. Liu, and S. Rohani. Effect of duty cycle and applied current frequency on plasma electrolytic oxidation (PEO) coating growth behavior. Surface and Coatings Technology, Vol. 226, 2013, pp. 100-107.
- [24] Wei, F., W. Zhang, T. Zhang, and F. Wang. Effect of variations of Al content on microstructure and corrosion resistance of PEO coatings on Mg Al alloys. Journal of Alloys and Compounds, Vol. 690, 2017, pp. 195-205.
- [25] Masiha, H., H. Bagheri, M. Gheytani, M. Aliofkhazraei, A. Rouhaghdam, and T. Shahrabi. Effect of nanocrystalline surface of substrate on microstructure and wetting of PEO coatings. Bulletin of Materials Science, Vol. 38, No. 4, 2015, pp. 935-943.
- [26] Martin, J., A. V. Nominé, J. Stef, A. Nominé, J. X. Zou, G. Henrion, et al. The influence of metallurgical state of substrate on the efficiency of plasma electrolytic oxidation (PEO) process on magnesium alloy. Materials & Design, Vol. 178, 2019, id. 107859.
- [27] Durdu, S., S. Bayramoğlu, A. Demirtaş, M. Usta, and A. H. Üçışık. Characterization of AZ31 Mg Alloy coated by plasma electrolytic oxidation. Vacuum, Vol. 88, 2012, pp. 130-133.
- Clyne, T. W. and S. C. Troughton. A review of recent work on [28] discharge characteristics during plasma electrolytic oxidation of various metals. International Materials Reviews, Vol. 64, No. 3, 2018, pp. 127-162.
- Mi, T., B. Jiang, Z. Liu, and L. Fan. Plasma formation mechanism [29] of microarc oxidation. Electrochimica Acta, Vol. 123, 2014, pp. 369-377.
- [30] Melnikov, O. A., E. A. Pecherskaya, P. E. Golubkov, G. V. Kozlov, and V. S. Alexandrov. Modeling of the dynamic current-voltage characteristic of micro-arc oxidation. St Petersburg Polytechnic University Journal: Physics and Mathematics, Vol. 68, No. 3.1, 2023, pp. 335-340.
- Shi, M. and H. Li. The morphology, structure and composition of [31] microarc oxidation (MAO) ceramic coating in Ca-P electrolyte with complexing agent EDTMPS and interpretation hypothesis of MAO Process. Electronic Processing of Materials, Vol. 52, No. 1, 2016,
- [32] Gazenbiller, E., S. Mansoor, N. Konchakova, M. Serdechnova, M. L. Zheludkevich, C. Blawert, et al. Computational damage modelling of PEO coated extruded magnesium tested in slow strain rate

- configuration. Surface and Coatings Technology, Vol. 446, 2022, id. 128758.
- [33] Torres-Huitzil, C. and B. Girau. Fault and error tolerance in neural networks: A review. IEEE Access, Vol. 5, 2017, pp. 17322-17341.
- [34] Netay, I. V.. Influence of digital fluctuations on behavior of neural networks. Indian Journal of Artificial Intelligence and Neural Networking, Vol. 3, No. 1, 2022, pp. 1-7.
- [35] Jin, S., X. Ma, R. Wu, G. Wang, J. Zhang, B. L. Krit, et al. Advances in micro-arc oxidation coatings on Mg-Li alloys. Applied Surface Science Advances, Vol. 8, 2022, id. 100219.
- [36] Kozelskaya, A. I., K. N. Verzunova, I. O. Akimchenko, J. Frueh, V. I. Petrov, G. B. Slepchenko, et al. Antibacterial calcium phosphate coatings for biomedical applications fabricated via micro-arc oxidation. Biomimetics, Vol. 8, No. 5, 2023, id. 444.
- [37] Ding, Z. Y., Y. H. Wang, J. H. Ouyang, Z. G. Liu, Y. M. Wang, and Y. J. Wang. Influence of Al2O3 addition in NaAlO2 electrolyte on microstructure and high-temperature properties of plasma electrolytic oxidation ceramic coatings on Ti2AlNb alloy. Surface and Coatings Technology, Vol. 370, 2019, pp. 187-195.
- [38] Bordbar-Khiabani, A., S. Ebrahimi, and B. Yarmand. Highly corrosion protection properties of plasma electrolytic oxidized titanium using rGO nanosheets. Applied Surface Science, Vol. 486, 2019, pp. 153-165.
- [39] Mohedano, M., R. Arrabal, B. Mingo, A. Pardo, and E. Matykina. Role of particle type and concentration on characteristics of PEO coatings on AM50 magnesium alloy. Surface and Coatings Technology, Vol. 334, 2018, pp. 328-335.
- [40] Fattah-alhosseini, A., R. Chaharmahali, and K. Babaei. Effect of particles addition to solution of plasma electrolytic oxidation (PEO) on the properties of PEO coatings formed on magnesium and its alloys: A review. Journal of Magnesium and Alloys, Vol. 8, No. 3, 2020, pp. 799-818.
- [41] Farshid, S. and M. Kharaziha. Micro and nano-enabled approaches to improve the performance of plasma electrolytic oxidation coated magnesium alloys. Journal of Magnesium and Alloys, Vol. 9, No. 5, 2021, pp. 1487-1504.
- [42] Molaei, M., M. Nouri, K. Babaei, and A. Fattah-Alhosseini. Improving surface features of PEO coatings on titanium and titanium alloys with zirconia particles: A review. Surfaces and Interfaces, Vol. 22, 2021, id. 100888.
- [43] Mamaev, A. I., Y. N. Dolgova, A. A. Yeltsov, G. V. Plekhanov, A. E. Ryabikov, T. A. Baranova, et al. Heterogeneous metal oxide coatings with magnetoactive nickel, cobalt, and iron phases formed by the method of pulsed microplasma oxidation for radiation absorption in the middle and near-IR regions. Russian Physics Journal, Vol. 63, No. 7, 2020, pp. 1265-1276.
- [44] Palanivel, M., R. Bhardwaj, L. Edalacheruvu, and N. Rameshbabu. Development of corrosion-resistant and hydrophobic coating on commercially pure titanium. Materials Today: Proceedings, Vol. 46, 2021, pp. 1017-1021.
- Amruthaluru, S., D. V. Pillai, H. Sampathirao, and N. Rameshbabu. [45] Development of plasma electrolytic oxidation coatings on Ti-42Al-2V-2Nb alloy. Materials Today: Proceedings, Vol. 46, 2021, pp. 1056-1060.
- [46] Farrakhov, R., O. Melnichuk, E. Parfenov, V. Mukaeva, A. Raab, V. Sheremetyev, et al. Comparison of biocompatible coatings produced by plasma electrolytic oxidation on cp-Ti and Ti-Zr-Nb superelastic alloy. Coatings, Vol. 11, No. 4, 2021, id. 401.
- [47] Guo, Y., L. Xu, J. Luan, Y. Wan, and R. Li. Effect of carbon nanotubes additive on tribocorrosion performance of micro-arc

- oxidized coatings on Ti6Al4V alloy. Surfaces and Interfaces, Vol. 28, 2022. id. 101626.
- [48] Sedelnikova, M. B., A. V. Ugodchikova, T. V. Tolkacheva, V. V. Chebodaeva, I. A. Cluklhov, M. A. Khimich, et al. Surface modification of Mg0.8Ca alloy via wollastonite micro-arc coatings: Significant improvement in corrosion resistance. Metals, Vol. 11, No. 5, 2021, id. 754.
- [49] Moga, S. G., D. A. Negrea, C. M. Ducu, V. Malinovschi, A. G. Schiopu, E. Coaca, et al. The influence of processing time on morphology, structure and functional properties of PEO coatings on AZ63 magnesium alloy. Applied Sciences, Vol. 12, No. 24, 2022, id. 12848.
- Tu, W., Z. Zhu, X. Zhuang, Y. Cheng, and P. Skeldon. Effect of frequency on black coating formation on AZ31 magnesium alloy by plasma electrolytic oxidation in aluminate-tungstate electrolyte. Surface and Coatings Technology, Vol. 372, 2019, pp. 34-44.
- Zhang, S., W. Guo, N. Liu, C. Xia, H. Wang, and C. Liang. In situ [51] preparation of MAO/TiO2 composite coating on WE43 alloy for anti-corrosion protection. Vacuum, Vol. 197, 2021, id. 110835.
- [52] Senocak, T. C., T. A. Yilmaz, H. F. Budak, G. Gulten, A. M. Yilmaz, K. V. Ezirmik, et al. Influence of sodium pentaborate (B5H10NaO13) additive in plasma electrolytic oxidation process on WE43 magnesium alloys. Materials Today Communications, Vol. 30, 2022, id. 103157.
- Lv, J. and Y. Cheng. Amorphous coatings on tantalum formed by plasma electrolytic oxidation in aluminate electrolyte and high temperature crystallization treatment. Surface and Coatings Technology, Vol. 434, 2022, id. 128171.
- [54] Wu, Y., Z. Yang, R. Wang, G. Wu, D. Chen, D. Wang, et al. An investigation of microstructure evolution for plasma electrolytic oxidation (PEO) coated Al in an alkaline silicate electrolyte. Surface and Coatings Technology, Vol. 351, 2018, pp. 136-152.
- [55] Rakoch, A. G., E. P. Monakhova, Z. V. Khabibullina, M. Serdechnova, C. Blawert, M. L. Zheludkevich, et al. Plasma electrolytic oxidation of AZ31 and AZ91 magnesium alloys: Comparison of coatings formation mechanism. Journal of Magnesium and Alloys, Vol. 8, No. 3, 2020, pp. 587-600.
- Dehnavi, V., X. Y. Liu, B. Luan, D. W. Shoesmith, and S. Rohani. Phase transformation in plasma electrolytic oxidation coatings on 6061 aluminum alloy. Surface and Coatings Technology, Vol. 251, 2014, pp. 106-114.
- [57] Liu, C., T. Xu, Q. Shao, S. Huang, B. Jiang, J. Liang, et al. Effects of beta phase on the growth behavior of plasma electrolytic oxidation coating formed on magnesium alloys. Journal of Alloys and Compounds, Vol. 784, 2019, pp. 414-421.
- [58] Matykina, E., R. Arrabal, M. Mohedano, B. Mingo, J. Gonzalez, A. Pardo, et al. Recent advances in energy efficient PEO processing of aluminium alloys. Transactions of Nonferrous Metals Society of China, Vol. 27, No. 7, 2017, pp. 1439-1454.
- [59] Xi, F., X. Zhang, Y. Kang, X. Wen, and Y. Liu. Mechanistic analysis of improving the corrosion performance of MAO coatings on Ti-6Al-4V alloys by annealing. Surface and Coatings Technology, Vol. 476, 2023, id. 130264.
- Rúa, J. M., A. A. Zuleta, J. Ramírez, and P. Fernández-Morales. [60] Micro-arc oxidation coating on porous magnesium foam and its potential biomedical applications. Surface and Coatings Technology, Vol. 360, 2019, pp. 213-221.
- [61] Liu, D., B. Jiang, Z. Liu, Y. Ge, and Y. Wang. Preparation and catalytic properties of Cu2O-CoO/Al2O3 composite coating

- prepared on aluminum plate by microarc oxidation. Ceramics International, Vol. 40, No. 7, 2014, pp. 9981–9987.
- [62] Alves, S. A., P. Fernández-Lopéz, A. Lopéz-Ortega, X. Fernández, I. Quintana, J. T. San-José, et al. Enhanced tribological performance of cylinder liners made of cast aluminum alloy with high silicon content through plasma electrolytic oxidation. Surface and Coatings Technology, Vol. 433, 2022, id. 128146.
- [63] Mingo, B., Y. Guo, A. Němcová, A. Gholinia, M. Mohedano, M. Sun, et al. Incorporation of halloysite nanotubes into forsterite surface layer during plasma electrolytic oxidation of AM50 Mg alloy. Electrochimica Acta, Vol. 299, 2019, pp. 772-788.
- [64] Fattah-alhosseini, A., M. Molaei, M. Nouri, and K. Babaei. Review of the role of graphene and its derivatives in enhancing the performance of plasma electrolytic oxidation coatings on titanium and its alloys. Applied Surface Science Advances, Vol. 6, 2021, id. 100140.
- [65] Attarzadeh, N. and C. V. Ramana. Plasma electrolytic oxidation ceramic coatings on zirconium (Zr) and Zr-alloys: Part-II: Properties and applications. Coatings, Vol. 11, No. 6, 2021, id. 620.
- [66] Wu, T., C. Blawert, M. Serdechnova, P. Karlova, G. Dovzhenko, D. C. Florian Wieland, et al. Formation of plasma electrolytic oxidation coatings on pure niobium in different electrolytes. Applied Surface Science, Vol. 573, 2021, id. 151629.
- [67] Blawert, C., S. A. Karpushenkov, M. Serdechnova, L. S. Karpushenkava, and M. L. Zheludkevich. Plasma electrolytic oxidation of zinc alloy in a phosphate-aluminate electrolyte. Applied Surface Science, Vol. 505, 2020, id. 144552.
- [68] Fattah-alhosseini, A., K. Babaei, and M. Molaei. Plasma electrolytic oxidation (PEO) treatment of zinc and its alloys: A review. Surfaces and Interfaces, Vol. 18, 2020, id. 100441.
- [69] Cheng, Y., B. Wei, Y. Liu, and Y. Cheng. Plasma electrolytic oxidation of copper in an aluminate based electrolyte with the respective additives of Na<sub>3</sub>PO<sub>4</sub>, NaH<sub>2</sub>PO<sub>4</sub> and NaH<sub>2</sub>PO<sub>2</sub>. Applied Surface Science, Vol. 565, 2021, id. 150477.
- [70] Nie, X., R. Cai, C. Zhao, J. Sun, J. Zhang, and D. T. A. Matthews. Advancement of plasma electrolytic oxidation towards non-valve metals. Surface and Coatings Technology, Vol. 442, 2022, id. 128403.
- [71] Buling, A. and J. Zerrer. Increasing the application fields of magnesium by ultraceramic®: Corrosion and wear protection by plasma electrolytical oxidation (PEO) of Mg alloys. Surface and Coatings Technology, Vol. 369, 2019, pp. 142-155.
- Jantimapornkij, P., J. Zerrer, and A. Buling. Advanced corrosion [72] protection of additive manufactured light metals by creating ceramic surface through CERANOD® plasma electrolytical oxidation process. Frontiers in Chemical Engineering, Vol. 3, 2021, id. 734644.
- [73] Kuznetsov, Y. A., M. A. Markov, A. V. Krasikov, R. Y. Bystrov, A. N. Belyakov, A. D. Bykova, et al. Formation of wear- and corrosionresistant ceramic coatings by combined technologies of spraying and micro-arc oxidation. Russian Journal of Applied Chemistry, Vol. 92, No. 7, 2019, pp. 875-882.
- [74] Qi, Y., S. Liu, L. Luo, Z. Peng, J. Liang, and P. Wang. Plasma electrolytic fluorination on Al alloys: Coating growth and plasma discharge behavior. Ceramics International, Vol. 47, No. 21, 2021, pp. 29758-29770.
- [75] Saji, V. S.. Review of rare-earth-based conversion coatings for magnesium and its alloys. Journal of Materials Research and Technology, Vol. 8, No. 5, 2019, pp. 5012-5035.
- [76] Sun, L., B. C. Zhao, T. Wang, J. Y. Cui, S. Zhang, F. Li et al. Surface characterization and corrosion resistance of biomedical AZ31 Mg

- alloy treated by microarc fluorination. Y. Zhao, editor. Scanning, Vol. 2020, No. 1, 2020, pp. 1-15.
- [77] Xue, L., C. Wu, H. Zhu, L. Yang, Z. Peng, Y. Liang, et al. Effect of ultra-audio frequency pulse energy on the growth mechanism and corrosion properties of Az31b ceramic coating by micro-arc oxidation. 2024. SSRN 4748728 [Internet]. https://papers.ssrn. com/sol3/papers.cfm?abstract\_id=4748728.
- **[78]** Hu, J., H. Li, X. Wang, L. Yang, M. Chen, R. Wang, et al. Effect of ultrasonic micro-arc oxidation on the antibacterial properties and cell biocompatibility of Ti-Cu alloy for biomedical application. Materials Science & Engineering, C: Materials for Biological Applications, Vol. 115, 2020, id. 110921.
- Kuroda, P. A. B., F. N. de Mattos, C. R. Grandini, and C. R. M. Afonso. Influence of the heat treatment temperature on the MAO coating produced in the Ti-25Ta-25Zr alloy. Journal of Materials Research and Technology, Vol. 26, 2023, pp. 3881-3892.
- [80] Chu, H. J., C. J. Liang, C. H. Chen, and J. L. He. Optical emission spectroscopic determination of the optimum regions for microarc oxidation of titanium. Surface and Coatings Technology, Vol. 325, 2017, pp. 166-173.
- [81] Chen, W., Z. Wang, L. Sun, and S. Lu. Research of growth mechanism of ceramic coatings fabricated by micro-arc oxidation on magnesium alloys at high current mode. Journal of Magnesium and Alloys, Vol. 3, No. 3, 2015, pp. 253-257.
- [82] Li, L., E. Yang, Z. Yan, X. Xie, W. Wei, and W. Li. Effect of preanodized film on micro-arc oxidation process of 6063 aluminum alloy. Materials, Vol. 15, No. 15, 2022, id. 5221.
- [83] Hussein, R. O., X. Nie, D. O. Northwood, A. Yerokhin, and A. Matthews. Spectroscopic study of electrolytic plasma and discharging behaviour during the plasma electrolytic oxidation (PEO) process. Journal of Physics D: Applied Physics, Vol. 43, No. 10, 2010, id. 105203.
- [84] Zhu, L., X. Ke, J. Li, Y. Zhang, Z. Zhang, and M. Sui. Growth mechanisms for initial stages of plasma electrolytic oxidation coating on Al. Surfaces and Interfaces, Vol. 25, 2021, id. 101186.
- [85] Malinovschi, V., A. Marin, C. Ducu, V. Andrei, E. Coaca, V. Craciun, et al. Influence of sodium aluminate concentration and process duration on microstructure, mechanical and electrochemical behavior of PEO coatings formed on CP-Ti. Surface and Coatings Technology, Vol. 418, 2021, id. 127240.
- [86] Moon, S. and Y. Jeong. Generation mechanism of microdischarges during plasma electrolytic oxidation of Al in aqueous solutions. Corrosion Science, Vol. 51, No. 7, 2009, pp. 1506-1512.
- [87] Kasalica, B., M. Petković-Benazzouz, M. Sarvan, I. Belča, B. Maksimović, B. Misailović, et al. Mechanisms of plasma electrolytic oxidation of aluminum at the multi-hour timescales. Surface and Coatings Technology, Vol. 390, 2020, id. 125681.
- Jangde, A., S. Kumar, and C. Blawert. Evolution of PEO coatings on [88] AM50 magnesium alloy using phosphate-based electrolyte with and without glycerol and its electrochemical characterization. Journal of Magnesium and Alloys, Vol. 8, No. 3, 2020, pp. 692-715.
- Dunleavy, C. S., I. O. Golosnoy, J. A. Curran, and T. W. Clyne. Characterisation of discharge events during plasma electrolytic oxidation. Surface and Coatings Technology, Vol. 203, No. 22, 2009, pp. 3410-3419.
- [90] Yasui, T., K. Hayashi, and M. Fukumoto. Behaviors of micro-arcs, bubbles, and coating growth during plasma electrolytic oxidation of β-titanium alloy. Materials, Vol. 16, No. 1, 2022, id. 360.
- [91] Mozafarnia, H., A. Fattah-Alhosseini, R. Chaharmahali, M. Nouri, M. K. Keshavarz, and M. Kaseem. Corrosion, wear, and antibacterial behaviors of hydroxyapatite/MgO composite PEO coatings

- on AZ31 Mg alloy by incorporation of TiO2 nanoparticles. Coatings, Vol. 12, No. 12, 2022, id. 1967.
- [92] Wang, C., F. Ma, P. Liu, J. Chen, X. Liu, K. Zhang, et al. The influence of alloy elements in Ti6Al4V and Ti35Nb2Ta3Zr on the structure, morphology and properties of MAO coatings. Vacuum, Vol. 157, 2018, pp. 229-236.
- [93] Rama Krishna, L. and G. Sundararajan. Aqueous corrosion behavior of micro arc oxidation (MAO)-coated magnesium alloys: A critical review. JOM, Vol. 66, No. 6, 2014, pp. 1045-1060.
- [94] Veys-Renaux, D. and E. Rocca. Initial stages of multi-phased aluminium alloys anodizing by MAO: Micro-arc conditions and electrochemical behaviour. Journal of Solid State Electrochemistry, Vol. 19, No. 10, 2015, pp. 3121-3129.
- [95] Lara Rodriguez, L., P. A. Sundaram, E. Rosim-Fachini, A. M. Padovani, and N. Diffoot-Carlo. Plasma electrolytic oxidation coatings on yTiAl alloy for potential biomedical applications. Journal of Biomedical Materials Research, Part B: Applied Biomaterials, Vol. 102, No. 5, 2013, pp. 988-1001.
- [96] Tillous, K., T. Toll-Duchanoy, E. Bauer-Grosse, L. Hericher, and G. Geandier. Microstructure and phase composition of microarc oxidation surface layers formed on aluminium and its alloys 2214-T6 and 7050-T74. Surface and Coatings Technology, Vol. 203, No. 19, 2009, pp. 2969-2973.
- [97] Walsh, F. C., C. T. J. Low, R. J. K. Wood, K. T. Stevens, J. Archer, A. R. Poeton, et al. Plasma electrolytic oxidation (PEO) for production of anodised coatings on lightweight metal (Al, Mg, Ti) alloys. Transactions of the IMF, Vol. 87, No. 3, 2009, pp. 122-135.
- [98] Chen, Y., S. Yang, W. Zhang, T. Zhang, and F. Wang. Influence of second phase on corrosion performance and formation mechanism of PEO coating on AZ91 Mg alloy. Journal of Alloys and Compounds, Vol. 718, 2017, pp. 92-103.
- [99] Lee, K. M., Y. G. Ko, and D. H. Shin. Effect of icosahedral phase on growth behavior of thin oxide film on MgZn12Y1.7 alloy via micro arc oxidation. Thin Solid Films, Vol. 531, 2013, pp. 261-265.
- [100] Jiang, B. L. and Y. M. Wang. Plasma electrolytic oxidation treatment of aluminium and titanium alloys. In: Surface Engineering of Light Alloys, Woodhead publishing, Cambridge, 2010, pp. 110–154.
- [101] Xue, Y., X. Pang, B. Jiang, H. Jahed, and D. Wang. Characterization of the corrosion performances of as-cast Mg-Al and Mg-Zn magnesium alloys with microarc oxidation coatings. Materials and Corrosion, Vol. 71, No. 6, 2019, pp. 992-1006.
- [102] Xia, Q., D. Zhang, D. Li, Z. Jiang, and Z. Yao. Preparation of the plasma electrolytic oxidation coating on MgLi alloy and its thermal control performance. Surface and Coatings Technology, Vol. 369, 2019, pp. 252-256.
- [103] Kim, S. P., M. Kaseem, and H. C. Choe. Plasma electrolytic oxidation of Ti-25Nb-xTa alloys in solution containing Ca and P ions. Surface and Coatings Technology, Vol. 395, 2020, id. 125916.
- [104] Yavari, S. A., B. S. Necula, L. E. Fratila-Apachitei, J. Duszczyk, and I. Apachitei. Biofunctional surfaces by plasma electrolytic oxidation on titanium biomedical alloys. Surface Engineering, Vol. 32, No. 6, 2016, pp. 411-417.
- [105] Guan, S., M. Qi, Y. Li, and W. Wang. Morphology evolution of the porous coatings on Ti-xAl alloys by Al adding into Ti during micro-arc oxidation in Na2B4O7 electrolyte. Surface and Coatings Technology, Vol. 395, 2020, id. 125948.
- [106] Yang, H., X. Wang, Z. Zhu, and R. Liu. Discharge characteristic of micro-arc oxidation on aluminum alloy under the changing electrolyte temperature. Journal of Materials Science and Chemical Engineering, Vol. 10, No. 11, 2022, pp. 24-35.

- [107] Xiong, D., P. Wang, X. Shen, J. W. Liu, B. Yang, Y. B. Gong, et al. Addition of LuCl3 for improving micro-structure and corrosion resistance of micro-arc oxidation coating formed on 6061. *International Journal of Electrochemical Science*, Vol. 16, No. 4, 2021, id. 210460.
- [108] Chen, Q., Z. Jiang, S. Tang, W. Dong, Q. Tong, and W. Li. Influence of graphene particles on the micro-arc oxidation behaviors of 6063 aluminum alloy and the coating properties. *Applied Surface Science*, Vol. 423, 2017, pp. 939–950.
- [109] Zhang, X., G. Cai, Y. Lv, Y. Wu, and Z. Dong. Growth mechanism of titania on titanium substrate during the early stage of plasma electrolytic oxidation. *Surface and Coatings Technology*, Vol. 400, 2020, id. 126202.
- [110] Shokouhfar, M. and S. R. Allahkaram. Effect of incorporation of nanoparticles with different composition on wear and corrosion behavior of ceramic coatings developed on pure titanium by micro arc oxidation. Surface and Coatings Technology, Vol. 309, 2017, pp. 767–778.
- [111] Wu, T., C. Blawert, M. Serdechnova, P. Karlova, G. Dovzhenko, D. C. Florian Wieland, et al. Role of phosphate, silicate and aluminate in the electrolytes on PEO coating formation and properties of coated Ti6Al4V alloy. *Applied Surface Science*, Vol. 595, 2022, id. 153523.
- [112] Gebert, A., D. Eigel, P. F. Gostin, V. Hoffmann, M. Uhlemann, A. Helth, et al. Oxidation treatments of beta-type Ti-40Nb for biomedical use. Surface and Coatings Technology, Vol. 302, 2016, pp. 88–99.
- [113] Dziaduszewska, M., M. Shimabukuro, T. Seramak, A. Zieliński, and T. Hanawa. Effects of micro-arc oxidation process parameters on characteristics of calcium-phosphate containing oxide layers on the selective laser melted Ti13Zr13Nb Alloy. *Coatings*, Vol. 10, No. 8, 2020, id. 745.
- [114] Tjiang, F., L. W. Ye, Y. J. Huang, C. C. Chou, and D. S. Tsai. Effect of processing parameters on soft regime behavior of plasma electrolytic oxidation of magnesium. *Ceramics International*, Vol. 43, 2017, pp. S567–S572.
- [115] Nashrah, N., M. P. Kamil, D. K. Yoon, Y. G. Kim, and Y. G. Ko. Formation mechanism of oxide layer on AZ31 Mg alloy subjected to micro-arc oxidation considering surface roughness. *Applied Surface Science*, Vol. 497, 2019, id. 143772.
- [116] Hafili, F., R. Chaharmahali, K. Babaei, and A. Fattah-alhosseini. Duty cycle influence on the corrosion behavior of coatings created by plasma electrolytic oxidation on AZ31B magnesium alloy in simulated body fluid. *Corrosion Communications*, Vol. 3, 2021, pp. 62–70.
- [117] Guo, H. F., M. Z. An, H. B. Huo, S. Xu, and L. J. Wu. Microstructure characteristic of ceramic coatings fabricated on magnesium alloys by micro-arc oxidation in alkaline silicate solutions. *Applied Surface Science*, Vol. 252, No. 22, 2006, pp. 7911–7916.
- [118] Laleh, M., A. S. Rouhaghdam, T. Shahrabi, and A. Shanghi. Effect of alumina sol addition to micro-arc oxidation electrolyte on the properties of MAO coatings formed on magnesium alloy AZ91D. *Journal of Alloys and Compounds*, Vol. 496, No. 1–2, 2010, pp. 548–552.
- [119] Golubkov, P. E., E. A. Pecherskaya, Y. V. Shepeleva, A. V. Martynov, T. O. Zinchenko, and D. V. Artamonov. Methods of applying the reliability theory for the analysis of micro-arc oxidation process. *Journal of Physics: Conference Series*, Vol. 1124, No. 8, 2018, id. 081014
- [120] Gunduz, K. O., Z. C. Oter, M. Tarakci, and Y. Gencer. Plasma electrolytic oxidation of binary Mg-Al and Mg-Zn alloys. *Surface and Coatings Technology*, Vol. 323, 2017, pp. 72–81.

- [121] de, O., F. G. S. Frutuoso, O. de, J. Vitoriano, and C. Alves-Junior.

  Controlling plasma electrolytic oxidation of titanium using current pulses compatible with the duration of microdischarges.

  Results in Materials, Vol. 15, 2022, id. 100310.
- [122] Wang, X. and F. Zhang. Influence of anions in phosphate and tetraborate electrolytes on growth kinetics of microarc oxidation coatings on Ti6Al4V alloy. *Transactions of Nonferrous Metals Society* of China, Vol. 32, No. 7, 2022, pp. 2243–2252.
- [123] Mortazavi, G., J. Jiang, and E. I. Meletis. Investigation of the plasma electrolytic oxidation mechanism of titanium. *Applied Surface Science*, Vol. 488, 2019, pp. 370–382.
- [124] Fatimah, S., Y. G. Kim, D. K. Yoon, and Y. G. Ko. Anomaly of corrosion resistance of pure magnesium via soft plasma electrolysis at sub-zero temperature. Surface and Coatings Technology, Vol. 385, 2020, id. 125383.
- [125] Lu, X., M. Mohedano, C. Blawert, E. Matykina, R. Arrabal, K. U. Kainer, et al. Plasma electrolytic oxidation coatings with particle additions A review. Surface and Coatings Technology, Vol. 307, 2016, pp. 1165–1182.
- [126] Xi, F., X. Zhang, X. Jiang, Y. Kang, X. Wen, and Y. Liu. Growth mechanism of oxide layer on Ti-6Al-4 V substrate with different surface topographies during the early stage of micro-arc oxidation. Surface and Coatings Technology, Vol. 467, 2023, id. 129685.
- [127] Li, P., Z. Yang, B. He, N. Wang, Y. Chen, Q. Zhao, et al. Effect of local "over-growth" on fracture behaviors of coated titanium fiber fabricated by plasma electrolytic oxidation. *Surfaces and Interfaces*, Vol. 36, 2023, id. 102645.
- [128] Yan, H., W. Liu, Y. Ma, T. Wang, L. Wu, L. Yang, et al. Effects of micro-arc oxidation process parameters on micro-structure and properties of Al<sub>2</sub>O<sub>3</sub> coatings prepared on sintered 2024 aluminum alloy. *Journal of Materials Engineering and Performance*, Vol. 33, No. 4, 2023, pp. 1862–1873.
- [129] Song, S., B. Chen, H. Li, R. Shi, C. Liu, B. Yang, et al. Growth behavior and insulation property of the oxide layer during microarc oxidation of aluminium in "soft" regime condition. *Journal of Materials Science*, Vol. 58, No. 16, 2023, pp. 7136–7148.
- [130] Liu, D. J., B. L. Jiang, M. Zhai, and Q. Li. Cu (II)-containing micro-arc oxidation ceramic layers on aluminum: Formation, composition, and catalytic properties. *Materials Science Forum*, Vol. 695, 2011, pp. 21–24.
- [131] Mamaev, A. I., Y. N. Dolgova, E. Y. Beletskaya, V. A. Mamaeva, and T. A. Baranova. Synthesis of nanostructured nonmetallic inorganic coatings at high energy localization in interfacial nanolayers. *Russian Physics Journal*, Vol. 63, No. 9, 2021, pp. 1605–1614.
- [132] Han, I., J. H. Choi, B. H. Zhao, H. K. Baik, and I. S. Lee. Micro-arc oxidation in various concentration of KOH and structural change by different cut off potential. *Current Applied Physics*, Vol. 7, 2007, pp. e23–e27.
- [133] Selvi, E., F. Muhaffel, Y. Yürektürk, A. S. Vanlı, and M. Baydoğan. Influence of electrolyte compositions and electrical parameters on thermal properties of micro-arc oxidized AZ91 alloy. *Journal of Materials Engineering and Performance*, Vol. 31, No. 2, 2021, pp. 1667–1678.
- [134] Wang, J., M. H. Du, F. Han, and J. Yang. Effects of the ratio of anodic and cathodic currents on the characteristics of micro-arc oxidation ceramic coatings on Al alloys. *Applied Surface Science*, Vol. 292, 2014, pp. 658–664.
- [135] Golubkov, P., E. Pecherskaya, O. Karpanin, M. Safronov, T. Zinchenko, and D. Artamonov. Development of theoretical foundations of the controlled synthesis of multifunctional

- coatings by the micro-arc oxidation method. *Proceedings of the XXth Conference of Open Innovations Association FRUCT*, Yaroslavl, Russia, 2020, pp. 1–11.
- [136] Galuza, A., I. Kolenov, D. Vinnikov, S. Mizrakhy, and A. Savchenko. Investigation of micro-arc oxidation coatings using sub-THz ellipsometry. *Materials Characterization*, Vol. 189, 2022, id. 111930.
- [137] Newman, J. and K. E. Thomas-Alyea. Electrochemical systems, John Wiley & Sons, Hoboken, New Jersey, 2012.
- [138] Kuznetsov, Y. A., M. A. Markov, I. N. Kravchenko, V. P. Lyalyakin, A. V. Krasikov, and A. D. Bykova. Thickness evaluation of ceramic coatings formed by microarc oxidation. *Metallurgist*, Vol. 64, No. 11–12, 2021, pp. 1300–1306.
- [139] Tousch, S., L. Magniez, S. Fontana, G. Marcos, C. Hérold, G. Henrion, et al. Influence of carbon nanotubes on the plasma electrolytic oxidation process of aluminum under "soft" sparking conditions. Surface and Coatings Technology, Vol. 468, 2023, id. 129779.
- [140] Hussein, R. O., X. Nie, and D. O. Northwood. An investigation of ceramic coating growth mechanisms in plasma electrolytic oxidation (PEO) processing. *Electrochimica Acta*, Vol. 112, 2013, pp. 111–119.
- [141] Yerokhin, A. L., A. Leyland, and A. Matthews. Kinetic aspects of aluminium titanate layer formation on titanium alloys by plasma electrolytic oxidation. *Applied Surface Science*, Vol. 200, No. 1–4, 2002, pp. 172–184.
- [142] Chu, Y., P. Liu, Y. Chen, and X. Li. Influence of applied voltage on surface morphology and wettability of biological coatings on Ti6-Al-4V by micro-arc oxidation treatment. *Materials Research*, Vol. 23, No. 1, 2020, id. 20200002.

- [143] Wang, J., H. Lu, Z. Sun, G. Xu, Z. Bai, and Z. Peng. Effect of ultra accurate control of electrolyte temperature on the performance of micro arc oxidation ceramic coatings. *Ceramics International*, Vol. 49, No. 20, 2023, pp. 33236–33246.
- [144] Fazel, M., H. Salimijazi, and M. Shamanian. Improvement of corrosion and tribocorrosion behavior of pure titanium by subzero anodic spark oxidation. ACS Applied Materials & Interfaces, Vol. 10, No. 17, 2018, pp. 15281–15287.
- [145] Khanmohammadi, H., S. R. Allahkaram, A. Igual Munoz, and N. Towhidi. The influence of current density and frequency on the microstructure and corrosion behavior of plasma electrolytic oxidation coatings on Ti6Al4V. *Journal of Materials Engineering and Performance*, Vol. 26, No. 2, 2017, pp. 931–944.
- [146] Zhang, Y., Q. Wang, R. Ye, and C. S. Ramachandran. Plasma electrolytic oxidation of cold spray kinetically metallized CNT-Al coating on AZ91-Mg alloy: Evaluation of mechanical and surficial characteristics. *Journal of Alloys and Compounds*, Vol. 892, 2022, id. 162094.
- [147] Rogov, A. B., Y. Huang, D. Shore, A. Matthews, and A. Yerokhin. Toward rational design of ceramic coatings generated on valve metals by plasma electrolytic oxidation: The role of cathodic polarisation. *Ceramics International*, Vol. 47, No. 24, 2021, pp. 34137–34158.
- [148] Aliasghari, S., P. Skeldon, and G. E. Thompson. Plasma electrolytic oxidation of titanium in a phosphate/silicate electrolyte and tribological performance of the coatings. *Applied Surface Science*, Vol. 316, 2014, pp. 463–476.